Smart Agricultural Technology 15 (2026) 102542

Contents lists available at ScienceDirect

Smart Agricultural Technology

journal homepage: www.journals.elsevier.com/smart-agricultural-technology

Integrating proximal soil sensing and Sentinel-1/2 remote sensing for management zone delineation and monitoring of variable-rate nitrogen fertilization in winter barley

Nazerke Amangeldy [a], Eduardo A. Garcia-Braga [d], Yasmina Chourak [c], Gerard Portal [d], Hongzhen Luo [b], Isi Bardají [d], Mercè Vall-llossera [d,e], Rosa Vilaplana Ventura [c], Antonios Morellos [a], Manuel Vázquez-Arellano [a], Erik Meers [b], Estefania Blanch [d], Abdul M. Mouazen [a,*]

[a] Department of Environment, Faculty of Bioscience Engineering, Ghent University, Ghent, Belgium
[b] Laboratory for Bioresource Recovery (Re Source Lab), Department of Green Chemistry and Technology, Faculty of Bioscience Engineering, Ghent University, Ghent, Belgium
[c] BETA Tech Centre (TECNIO Network), University of Vic-Central University of Catalonia, Ctra. de Roda 70, VIC, 08500, Spain
[d] Institut d'Estudis Espaials de Catalunya (IEEC), Parc UPC - PMT, Edif. RDIT, Carrer d'Esteve Terradas, 1, Castelldefels, Barcelona, 08860, Spain
[e] CommSensLab, Signal Theory and Communications, Universitat Politècnica de Catalunya (UPC), Campus Nord UPC, Barcelona, 08034, Spain

ARTICLE INFO

Dataset link: https://dataspace.copernicus.eu/

Keywords:
SAR (synthetic aperture radar)
Winter barley
Nitrogen
Agriculture
Sentinel-1 and Sentinel-2

ABSTRACT

Uniform nitrogen (N) fertiliser (URNF) application is inefficient where soils vary within a field, driving avoidable economic and environmental losses. Variable-rate N fertiliser (VRNF) application can reallocate N to match this variability, but a practical framework for monitoring crop growth response to VRNF in the field is lacking. Therefore, a crop growth monitoring framework combining Sentinel-2 (S2) optical and Sentinel-1 (S1) C-band Synthetic Aperture Radar (SAR) observations was assessed to evaluate VRNF relative to the farmer's URNF application practice in three commercial winter barley fields in Catalonia (Spain). Two VRNF strategies, namely, King's (VRNF-KS) and Robin Hood (VRNF-RHS), were evaluated against URNF practice. Spatio-temporal clustering of S2 and S1 time series was utilized to evaluate satellite sensitivity to within-field heterogeneity of soil properties identified by proximal soil sensing (PSS), while simultaneously monitoring treatment-specific (VRNF and URNF) crop growth. The two VRNF strategies produced contrasting outcomes. VRNF-RHS improved both yield (+0.21 t ha^{-1}) and gross margin (+41.15 EUR ha^{-1}) relative to URNF, while applying marginally less N, outperforming both URNF and VRNF-KS agronomically and economically. VRNF-KS prioritised input reduction, achieving an N saving but incurring a slight yield penalty (-0.20 t ha^{-1}) and a gross-margin loss (-34.54 EUR ha^{-1}). The yield did not differ significantly among treatments ($p = 0.116$), indicating that these economic differences emerged despite statistically comparable yields. Cross-consistency analysis revealed consistently low agreement (overall agreement < 34%) between satellite-derived and PSS-derived management zone maps, indicating that S2 optical and S1 SAR signals reflecting realised crop conditions rather than underlying edaphic potentials. The broadband S2 indices differentiated treatments only weakly, whereas S1 VH/VV captured treatment-associated canopy heterogeneity more distinctly, suggesting that SAR may be a more sensitive indicator of VRNF-driven within-field variability, though this reflected greater dispersion rather than a statistically significant separation within a single season. Overall, freely available Sentinel-2 optical and Sentinel-1 SAR data can complement proximal soil sensing to support operational, site-specific nitrogen management in Mediterranean cropping systems, although multi-site and multi-year validation is still needed.

* Corresponding author.
E-mail address: Abdul.Mouazen@UGent.be (A.M. Mouazen).

https://doi.org/10.1016/j.atech.2026.102542
Received 29 April 2026; Received in revised form 2 September 2026; Accepted 3 September 2026
Available online 3 September 2026
2772-3755/© 2026 The Author(s). Published by Elsevier B.V. This is an open access article under the CC BY license (http://creativecommons.org/licenses/by/4.0/).

1. Introduction

Increasing exposure of agricultural croplands to climate extremes such as heat waves, and droughts heightens pressures on production systems and rural livelihoods. Isolated daily extreme weather events may have a limited immediate impact on individual farmers; however, several years of and further prolonged abrupt shifts in temperature and rainfall patterns systematically erode farmers' economic resilience. In this context, optimal nitrogen (N) input remains a major focus, primarily due to agronomic and environmental concerns associated with N losses. The N deficiency can impair crop growth because of its essential role in photosynthesis processes and growth-development of crops [1]. On average, only about 66–69% of applied N is typically taken up by arable crops in European countries [2], while the remainder is prone to nitrate (NO_3^-) leaching, which endangers aquatic ecosystems, and to nitrous oxide (N_2O) emissions, one of the main concern greenhouse gasses (GHG) directly driving climate change [1,3]. Although N use efficiency (NUE) in European countries is relatively higher than in China or India (i.e., stricter environmental and fertilizer regulations, country or even region-specific fertilizer recommendations systems), there is a need to expand the adoption of site-specific farming technologies along with crop diversification strategies to further enhance the NUE at the farm scale [2,3]. Therefore, '5Rs' approach of applying the right source, at the right rate, at the right time, in the right place, with the right technology, takes local farming conditions into account, while aiming to secure profitable outcomes for farmers [2,4] and reduce environmental impacts from excess use of synthetic fertilisers. This concept also feeds into the European Union (EU) Common Agricultural Policy (CAP) strategic plans, which promote the adoption of precision farming tools among farmers [5]. Further, mapping the spatial and temporal dynamics of agricultural croplands with today's freely accessible remote sensing data, from the EU Copernicus Sentinel-1 (S1) C-band Synthetic Aperture Radar (SAR) and Sentinel-2 (S2) optical satellite missions, together with information from ground-based sensing technologies, can provide management insights that support farmer's decision-making. In this context, S2 remote sensing has become widely used for monitoring of agricultural crops, whose output (e.g., NDVI, normalised difference vegetation index) is commonly adopted into variable-rate N fertilizer (VRNF) applications when combined with proximal soil sensing (PSS) derived soil fertility attributes [6–11]. However, research and operations in (precision) agriculture are increasingly moving toward multi-sensor approaches to compensate for known limitations in optical-only monitoring [12,13]. Additionally, optical time series also suffers from cloud-driven gaps that can disrupt time series agronomic monitoring. In this context, S1 SAR can help to close such gaps as it operates day and night in all weather, and its backscatter is sensitive not only to vegetation amount but also to canopy structure, dielectric properties, and water content [14,15]. However, utilisation of the full potential of S1 SAR data remains comparatively underexplored, especially for VRNF application in croplands [14,16–18]. Furthermore, methodological reports on site-specifically derived data remains limited: soil heterogeneity is routinely acknowledged, yet VRNF and uniform rate N fertiliser (URNF) effects are typically summarised through treatment averages, leaving their spatial correspondence with within-field soil and crop variability unresolved [6,19]. We address this through implementing cross-consistency analysis [20,21], which to our knowledge has not previously been used to evaluate spatial allocations on N fertiliser against site-specific yield, soil texture and PSS-derived management zones (MZs/MZD) relative to S1/S2 satellite observations.

In this study, a crop growth monitoring framework combining S2 optical and S1 C-band SAR observations was evaluated for VRNF against the farmer's URNF practice in three commercial winter barley fields in Catalonia, Spain. The specific objectives of this study are to (i) quantify the agronomic and economic response to VRNF relative to the farmer's conventional URNF practice, in terms of yield, soil physical properties, N input, and gross margin; (ii) assess the ability of S2 spectral indices and S1 backscatter metrics to capture treatment-specific winter barley growth dynamics, including their sensitivity in separating VRNF and URNF; and (iii) determine whether satellite sensing-derived crop growth spatio-temporal patterns are consistent with, or diverge from, the site-specific PSS-derived MZD, soil texture, and yield, which together represent within-field soil and crop variability.

2. Materials and methods

2.1. Workflow

The overall workflow of the study is summarized in Fig. 1. The methodology follows a sequential framework integrating PSS-derived MZD with optical and radar satellite remote sensing; individual steps detailed in the following sections. A tractor-mounted, on-line soil scanning with a visible and near-infrared (vis-NIR) spectroscopy was conducted concurrently with randomized, site-specific soil sampling. Samples were analysed in the laboratory for key fertility parameters, and these measurements served as target variables to calibrate and validate partial least squares regression (PLSR) models, translating the high-resolution vis-NIR spectra into continuous maps of soil properties. Data fusion and raster analysis were then combined with k-means clustering to delineate MZs, which formed the basis for site-specific N fertilisation prescription maps (PMs). Crop vigour and growth responses were monitored throughout the season using a combined S1 radar and S2 optical time series. The VRNF was evaluated against conventional URNF baselines in terms of agronomic performance (yield, fertiliser use efficiency), economic outcomes (cost analysis), and treatment-specific spatio-temporal dynamics derived from S1 radar and S2 optical sensors (spatial dissonance). Cross-consistency analysis was applied to compare the spatial patterns of site-specific yield, soil texture and PSS-derived MZD against fused S1/S2 crop growth variability. The key field operations included PSS and site-specific soil sampling for soil characterization on 9th of October 2024, sowing on 21stof November 2024, VRNF on 25th of February 2025, and harvest on 13th of June 2025.

2.2. Study area

The study was conducted within the municipality of Òdena, Catalonia (north-eastern Spain). The municipality spans approximately 52.66 km^2 and lies at a mean elevation of about ~421 m above sea level. According to the COoRdination of INformation on the Environment (CORINE) Land Cover inventory [22], the landscape is dominated by heterogeneous mosaics of non-irrigated arable land and mixed agricultural areas intermixed with forest and shrubland, while artificial surfaces are mainly confined to the urban nucleus, transportation roads and the nearby aerodrome. The three sites investigated comprise 14.3 ha of agricultural parcels located near Odena, centred at approximately 41.578,858° N, 1.659,332° E (Fig. 2).

The climate is classified as inland Mediterranean, characterized by hot, dry summers and cool to mild winters, with precipitation mainly centred in spring and autumn. Based on the 1991–2020 reference period, mean annual precipitation is 554 ± 144 mm and mean annual temperature is 14.1 °C, with mean summer daily maxima reaching 30–32 °C and winter minima approaching 0 °C with an average of approximately 59 frost days per year (Igualada/Òdena station[23]).

The crop rotation in all selected parcels comprised wheat in 2022, followed by winter barley in 2023 and 2024. The fields were managed under no-tillage system, with crops established by direct drilling; together, these represent the farmer's standard management practice. Winter barley management for the 2024–2025 season, reflecting typical local practice, is summarized in Fig. 3.

2.3. On-line soil scanning and laboratory analysis

A multi-sensor on-line soil scanning platform described by Mouazen

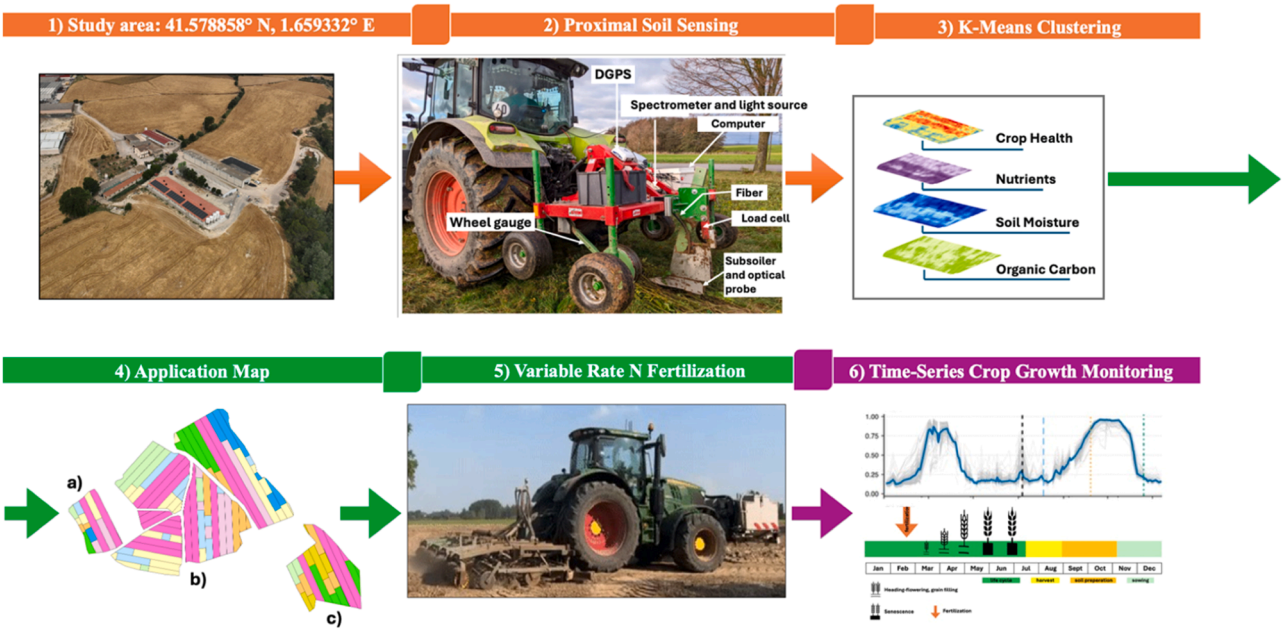


Fig. 1. Overview of the study workflow, showing the progression from tractor-mounted proximal soil sensing (PSS) platform (2), mapping and k-means clustering to produce management zones (MZs; 3) and strip experiment maps (4), to field implementation of nitrogen fertilisation and finally the use of time-series for crop growth monitoring comparing variable rate N fertilisation (VRNF) with uniform rate N fertilisation (URNF) treatments.

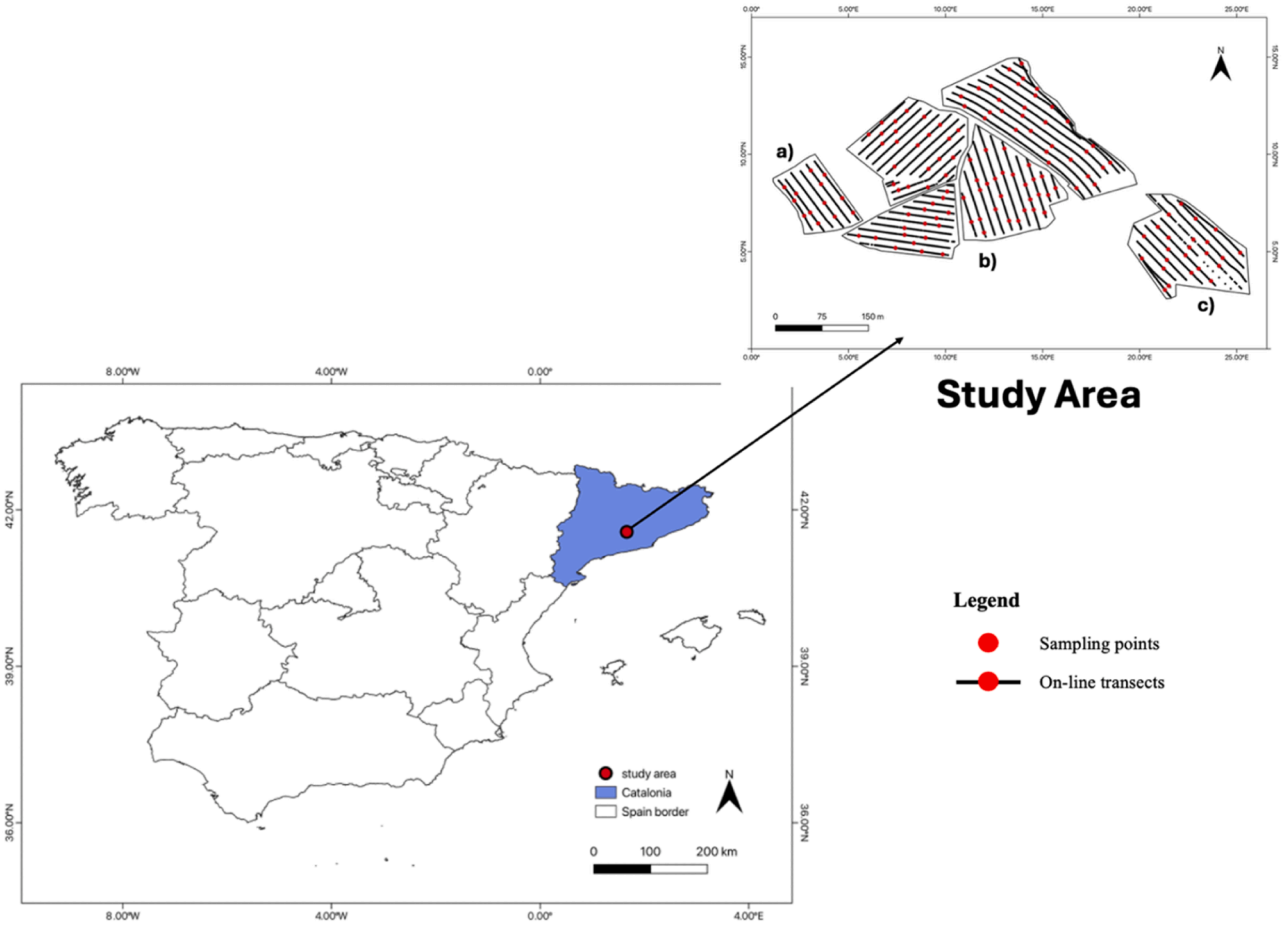


Fig. 2. Geographic location of the study area, comprising three fields near Odena, north-eastern Spain. The maps show also on-line soil scanning transects and sampling points.

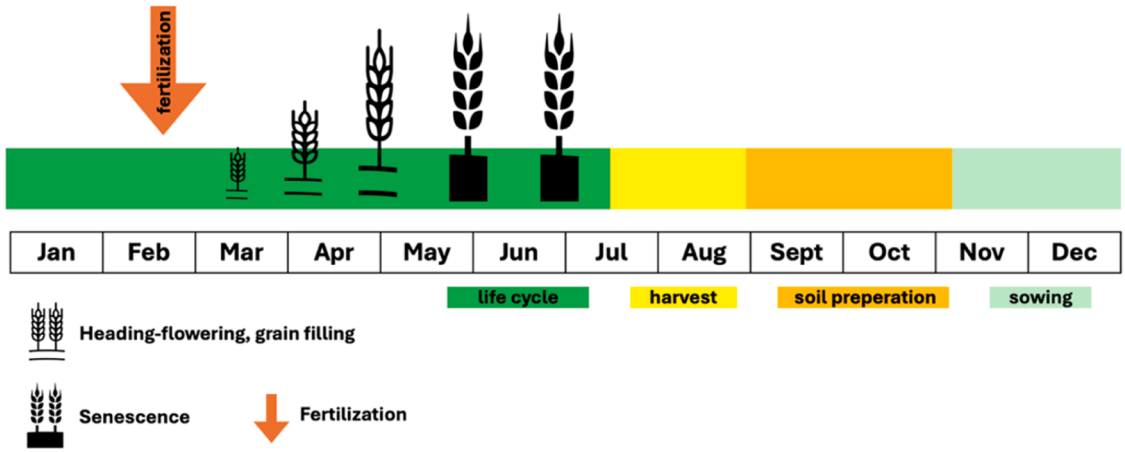


Fig. 3. Farmer's knowledge-based growth stages of winter barley in Òdena (Catalonia), with associated periods of management practices, and the indicative timing of transitions between crop growth stages.

[24] was used for PSS, simultaneously acquiring vis-NIR spectra (305–1700 nm). Centimetre-accuracy positioning was provided by a Trimble NAV-900 GNSS receiver with RTX® correction. The platform (panel 2 in Fig. 1) is equipped with a subsoiler that opens a ~6 cm wide trench at 15–25 cm depth; the bottom of this trench is smoothed so that a fiber-optic probe, connected to a Tec5 vis-NIR spectrometer, can collect soil spectra from the freshly exposed soil face. A 100% ceramic reference was measured every 30 min to correct for instrumental drift and environmental variation. All sensors' data were logged synchronously at 1 Hz using a NI CompactRIO 9082 running in LabVIEW. Further details on the sensor components and scanning procedures are given in Guerrero et al. [8]. During autumn 2024, the platform was tractor-pulled along parallel transects 12 m apart at ~3.5 km h^{-1} and a working depth of ~25 cm. A total of 138 soil samples were randomly collected from the trench bottom for model calibration and validation. After the field scanning and sampling, the soil samples were placed in a portable cooler with ice packs, transported to Ghent (Belgium) and delivered to the Soil Service of Belgium (BDB, Heverlee, Belgium) for analysis of pH, total N (TN), soil organic carbon (SOC), plant-available phosphorous (P_{AL}), and exchangeable potassium (K_{ex}), magnesium (Mg_{ex}), calcium (Ca_{ex}), and sodium (Na_{ex}). SOC was measured by dry combustion following the Dumas principle (ISO 10694; CMA/2/II/A.7; BOC). Soil $pH_{(KCl)}$ was measured in the supernatant, after shaking and equilibration for 2 h in mol/l potassium chloride solution (KCl), using 1:2.5 soil:solution ratio. K_{ex}, Mg_{ex}, Ca_{ex}, and Na_{ex} were quantified in ammonium lactate extract using ICP-AES (ISO 11885; CMA2/I/B1). P_{AL} was extracted and analysed according to BAM part 1/11 (BDB, Heverlee, Belgium). Gravimetric soil moisture content (MC) was obtained by oven-drying at 105 °C for 24 h. Cation exchange capacity by bases (CEC_B) was calculated as the sum of available Ca^{2+}, K^+, Mg^{2+} and Na^+ [25, 26]. TN was quantified by dry combustion using an elemental analyser in accordance with UNE 77325:2003. Soil texture (silt, clay and sand in %) was determined for 13 samples, selected randomly from the 138 soil samples collected in 2024, using the Robinson-Köhn pipette method [27]. Bulk density (BD) in g cm^{-3} was determined by the oven drying method at 105 °C for 24 h, whose samples were collected randomly from selected 75 sampling points (Section 3.2).

2.4. Diffuse reflectance spectral modelling

Spectral data were first pre-processed by applying splice-correction at the 1045 nm detector junction [28], trimming noisy end-bands, resulting in effective spectral windows between 350 and 1690 nm that varied according to the soil property of interest. Then smoothing with a Savitzky-Golay (second-order polynomial, 5-point window) filter was carried out, followed by standard normal variate (SNV) normalization [29]. Each dataset was split into 70% and 30% via the Kennard-Stone algorithm [30] to form calibration and validation subsets, respectively. PLSR was utilized to predict the selected soil properties (TN, SOC, MC, P_{AL}, K_{ex}, Mg_{ex}, Na_{ex}, Ca_{ex} and CEC_B). Model accuracy was assessed by using the ratio of performance to deviation (RPD) and the ratio of performance to interquartile distance (RPIQ), both of which are widely recognized indicators of model-performance, with the latter being more robust and reliable [31]. Prediction accuracy was classified based on RPIQ values as excellent (RPIQ > 2.5), very good (2.0–2.5), good (1.7–2.0), fair (1.4–1.7), and poor (RPIQ < 1.4) [32]. All spectral pre-treatment and PLSR modelling were performed in Jupyter Notebook (v6.5.2) using Python (v3.10.8).

For geospatial interpolation, the study area was subdivided into three distinct zones (Table 1). This subdivision was primarily motivated by the relatively large geographical separation of two of these zones (Section 2.5: a and c in Fig. 4) from the remaining area. Prior to using the on-line spectra for predicting the above-listed soil properties, trained 1-dimenstional convolutional neural network (1D CNN) model by Amangeldy et al. [33] was used to flag and exclude outliers and non-soil spectra. The 1D CNN classifier model was trained on 11,925 on-line vis-NIR spectra acquired with the same multi-sensor platform [24] and Tec5 spectrometer (305–1700 nm), manually labelled as 'soil' (6724) and 'non-soil' (5201), spectra. Spectra were pre-processed (noisy-edge, elimination, detector joint-jump correction, normalization) and transformed into 1D inputs (1201 wavelengths) via standard normal variate (SNV) normalization. The network comprises two 1D convolutional layers (64 filters, kernel size = 3; and 160 filters, kernel size = 10; both rectified linear unit [ReLU]) with intervening max-pooling (size = 3), followed by global average pooling, dropout (0.5), a dense layer (128 units, ReLU), and a sigmoid output returning a soil and non-soil probability. It was trained on Adam optimizer (learning rate 0.01) for up to 160 epochs (batch size = 32, early stopping patience = 35). The trained 1D CNN classifier flagged and excluded non-soil and outlier spectra. In addition, two-rule-based pre-checks discarded clearly non-soil spectra

Table 1
Site description of selected three study fields, showing the texture types according to the United State Department of Agriculture (USDA).

Field name	Area (ha)	Clay (%)	Sand (%)	Silt (%)	Texture (USDA)	Previous crop
Field-1 (a)	1.26	39.71 (± 6.11)	17.26 (± 9.04)	43.03 (± 6.52)	clay	winter barley
Field-2 (b)	10.51	41.27 (± 9.74)	15.61 (± 11.23)	43.12 (± 4.62)	silty clay	
Field-3 (c)	2.53	45.23 (± 5.02)	16.14 (± 6.65)	38.63 (± 1.91)	clay	

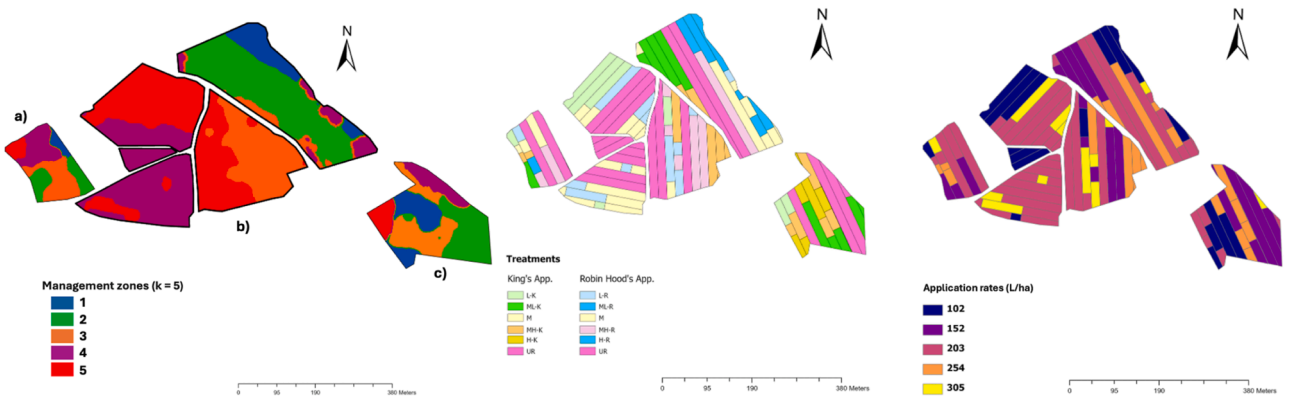


Fig. 4. Comparison of variable rate nitrogen (N) king's scheme (VRNF-KS) and variable rate N Robin Hood scheme (VRNF-RHS) of nitrogen (N) fertilizer (VRNF) application strategies. Left: management zone (MZ) map derived from on-line proximal soil-sensing (PSS) data via k-means clustering ($k = 5$), with the study area divided into Field-1 (a), Field-2 (b; bold outline), and Field-3 (c). Centre: N parallel-strip application maps for each strategy i.e., VRNF-RHS assigns lower N rates to more fertile zones; VRNF-KS assigns higher rates to more fertile zones. Right: resulting VRNF prescription map. Application classes are denoted by low fertility (L), medium low (ML), medium (M), medium high (MH), high (H); UR denotes the uniform-rate reference.

before model call, reference $\geq$ 60% within the first 200 bands, or $\leq$ 7.5% within 600–900 nm, with classifier applied only two spectra meeting neither condition. On the independent validation set, the classifier achieved an accuracy of 99.43% and an F1-score of 99.50%.

The on-line vis-NIR spectra remaining after 1D CNN filtering were used to predict soil properties using the validated PLSR calibration

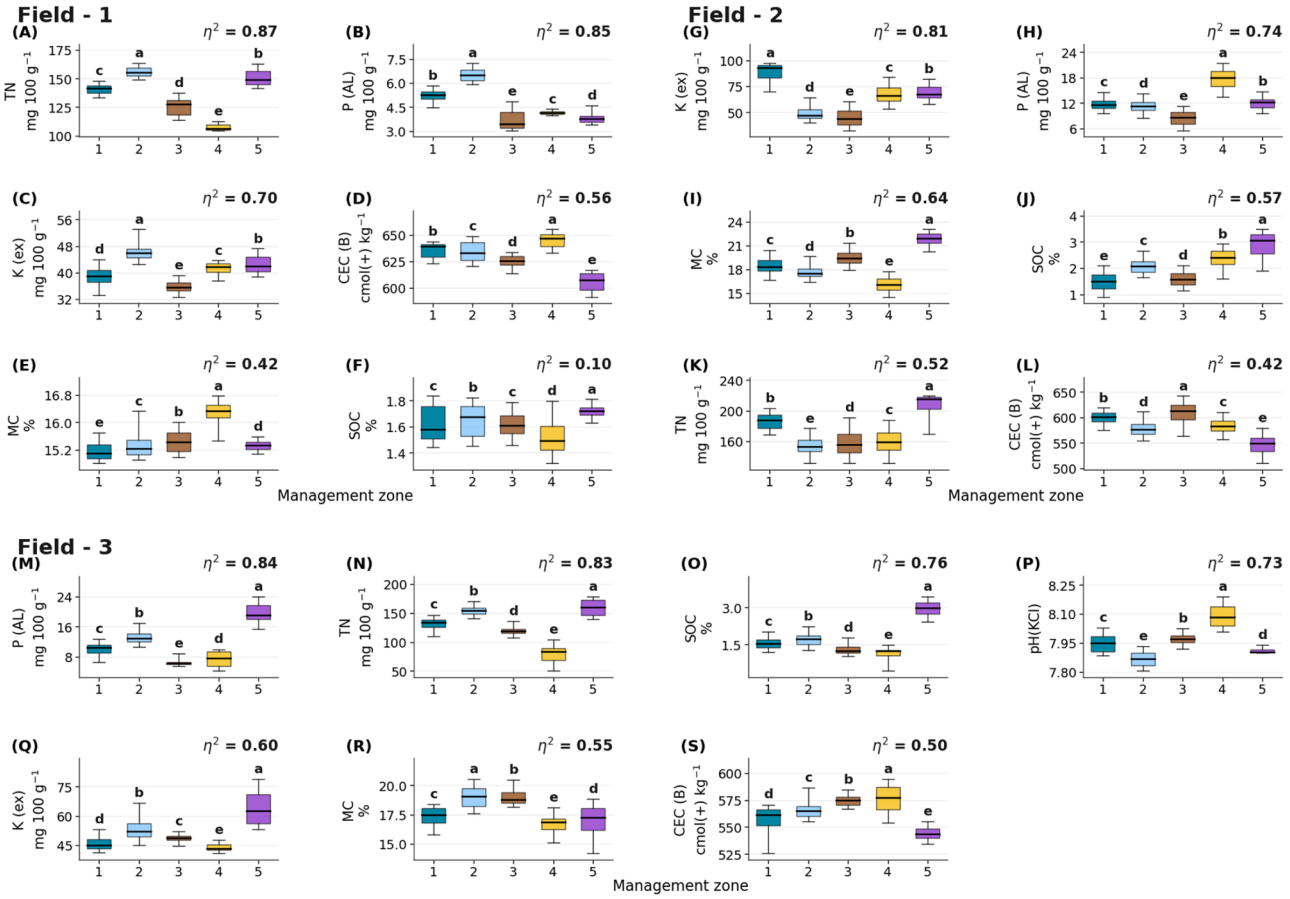


Fig. 5. Distribution of soil properties across five management zones (MZs) delineated independently in each of three fields. Field 1 comprises (A) total nitrogen (TN), (B) phosphorous (P_{AL}), (C) extractable potassium (K_{ex}), (D) cation exchange capacity (CEC_B), (E) moisture content (MC), and (F) soil organic carbon (SOC). Field 2 comprises (G) K_{ex}, (H) P_{AL}, (I) MC, (J) SOC, (K) TN, and (L) CEC_B. Field 3 comprises (M) P_{AL}, (N) TN, (O) SOC, (P) $pH_{(KCl)}$, (Q) K_{ex}, (R) MC, and (S) CEC_B. Panels within each field are ordered by decreasing descriptive effect size, η^2, which is shown above each panel and represents the proportion of observed variance in that property associated with management zone (MZ, $k = 5$). Lowercase letters show Games-Howell compact-letter groupings following Welch's heteroscedastic one-way analysis of variance (ANOVA); MZs sharing at least one letter within a panel were not significantly different at $\alpha = 0.05$. The observations are spatially autocorrelated interpolated raster pixels rather than independent field samples, so the *p*-values and letter groupings are likely to be anti-conservative. The properties shown were also inputs to the k-means clustering; consequently, these comparisons describe the clustering solution rather than independently validating the MZs.

models. The measured and predicted soil property values, together with general descriptive statistical analyses, are provided in Table A.1 (Appendix A). The parameters calculated include mean, standard deviation (SD), minimum (min), maximum (max), coefficient of variation (CV, %), skewness, and kurtosis.

2.5. Management zone maps

MZ maps were defined by integrating on-line predicted soil properties (see Appendix A). An exception was Field-3 (c in Fig. 4), where steep slope imposed operational constraints on the tractor-mounted on-line sensing equipment (limited traction and stability during scanning); MZ delineation (MZD) at this site was therefore based on the 27 available soil sampling points. A raster analysis was implemented to resample all soil properties to a common 5 × 5 m grid in ArcMap(v10.8.2)/ArcGISPro (v3.4.5) software (Esri, Environmental Systems Research Institute, Redlands, California, USA). All spatial mapping analyses were performed using Esri software accesses between 2023 and 2025. Each field was clustered separately (Fig. 5). Properties were retained as clustering inputs only where both requirements were met simultaneously per field: the property is essential for crop growth, and it exhibited spatial heterogeneity within the field. On this basis, the inputs were the resampled rasters of SOC, TN, P_{AL}, K_{ex}, CEC_B and MC for Fields 1 and 2, and the same six properties plus $pH_{(KCl)}$ for Field 3, each range-normalised to [0, 1]. K-means clustering ($k = 5$) in RStudio (RStudio Inc, USA) was used to group each field into zones with internally similar soil conditions. In the absence of site-specific yield data from previous seasons, cluster selection was informed by integrated soil properties (Appendix A), and farmer's field-knowledge to ensure agronomic relevance [6]. Also, final cluster selection prioritized spatial coherence to eliminate fragmented "salt-and-pepper" distributions, hence optimal k was set to five clusters. Treatment allocation followed partially predefined management guidelines for allocating the "Robin Hood scheme" (RHS) and "King's scheme" (KS) treatments. Field-3 (c) was assigned exclusively to the KS, while in the remaining parts of the study area both approaches were allocated at random in combination with the MZ map patterns as shown in Fig. 4.

2.6. Fertilization treatments

In VRNF, a key management question is whether higher N rates should be directed to the most fertile zones (KS) or to the least fertile zones (RHS). In this study, both approaches were implemented and compared. The RHS strategy allocated higher N doses to low-fertility zones and reduced doses to high-fertility zones, whereas the KS strategy did the opposite by increasing N in high-fertility zones and decreasing it in low-fertility zones. In addition, the URNF treatment was imposed in a spatially randomized manner across the selected fields. Both VRNF schemes (RHS and KS) were operationalised as discrete N levels around the farmer's recommended baseline rate (R) of 203 L ha^{-1}, applied using VR fertiliser technology into 18 m wide subdivided strips. This enabled a direct comparison of the two spatial N allocation strategies (RHS vs. KS) in terms of the agronomic and economic performance of winter barley. VRNF was applied at five levels relative to the uniform reference ($R = 203$ L ha^{-1}, 100%): low (L = 102 L ha^{-1}, 50% of R), medium-low (ML = 152 L ha^{-1}, 75%), medium (M = 203 L ha^{-1}, 100%), medium-high (MH = 254 L ha^{-1}, 125%), high (H = 305 L ha^{-1}, 150%). All VRNF treatments were evaluated against the URNF control (Table 2). The ± 50% range in 25% increments was chosen to span the agronomically plausible variation around the farmer's baseline R, while remaining acceptable to the growers and consistent with the applicator's resolution at 18 m working width (Table D.1; Appendix D).

For both URNF and VRNF treatments, N-based fertilizer used in this trial was Nitro Azufre 32, a liquid N-S solution labelled as "N solution with S 24 (8)," containing 24% w/w total N and 8% w/w SO_3. N was supplied as 2% nitrate-N, 6% ammonium-N, and 16% urea-N, with the sulphur (S) fraction (as SO_3) fully water-soluble. The product is a semi-transparent, slightly yellow liquid with the following characteristics: density = 1.23 ± 0.02 kg L^{-1} at 20 °C; pH = 7 ± 1.

Table 2
Overview of nitrogen (N) fertilizer treatments and application rates applied across the study area.

Field label	Treatment	Fertilizer type	N content (%)	N rate (L ha^{-1})	Application zones
Field-1 (a)	URNF	synthetic (Nitro Azufre 32)	24	203	2 uniform strips
	VRNF-KS	synthetic (Nitro Azufre 32)	24	102–305	5 MZs (VR-H to VR-L)
	VRNF-RHS	synthetic (Nitro Azufre 32)	24	305–102	5 MZs (VR-L to VR-H)
Field-2 (b)	URNF	synthetic (Nitro Azufre 32)	24	203	16 uniform strips
	VRNF-KS	synthetic (Nitro Azufre 32)	24	102–305	5 MZs (VR-H to VR-L)
	VRNF-RHS	synthetic (Nitro Azufre 32)	24	305–102	5 MZs (VR-L to VR-H)
Field-3 (c)	URNF	synthetic (Nitro Azufre 32)	24	203	3.5 uniform strips
	VRNF-KS	synthetic (Nitro Azufre 32)	24	102–305	5 MZs (VR-H to VR-L)
	VRNF-RHS	synthetic (Nitro Azufre 32)	24	305–102	5 MZs (VR-L to VR-H)

URNF, uniform-rate nitrogen fertilizer (Nitro Azufre 32); VRNF-KS, variable-rate kings' scheme targeted strategy (higher N to high-fertility zones); VRNF-RHS, variable-rate Robin Hoods targeted strategy (higher N to low-fertility zones); MZ, management zone. Variable-rate levels, from highest to lowest, are high (VRNF-H), medium-high (VRNF-MH), medium (VRNF-M), medium-low (VRNF-ML) and low (VRNF-L); the parenthetical in the "Application zones" column indicates the rate-to-zone mapping. Fertiliser strips were 18 m wide. Fertilization was applied once.

2.7. Site-specific application and yield map

Barley yield was measured with a combine harvester equipped with a yield monitoring system. However, raw yield data inherently contains systematic machine errors and localized spatial noise. To extract true agronomic yield, a two-stage outlier detection algorithm was applied to the dataset (see Appendix B). First, an initial deterministic filtering pass was conducted to eliminate artificial yield fluctuations caused by combine harvester operation. Yield points were classified as mechanical anomalies and removed from the dataset if they violated standard operational thresholds derived from the machinery telemetry:

(i) incomplete swath: header width recorded below 5.0 m,
(ii) velocity anomalies: combine speed falling outside the optimal harvesting range of 0.5 to 6.0 km h^{-1}, indicative of sudden stops, turns, or non-harvesting transit,
(iii) sensor glitches: grain moisture readings outside biologically realistic bounds (<3.0% to >20.0%).

Following the removal of mechanistic artifacts, a moving-window spatial filter was employed to identify and remove localized yield anomalies (e.g., sudden material flow disruptions), while preserving the natural spatial variability of the field. For each data point, a local neighbourhood was established using a 15 m search radius, computed

via a KD-Tree spatial index. If the neighbourhood contained a minimum of 10 points, the local mean (μ_{local}) and sample standard deviation (σ_{local}) were calculated to prevent the false deletion of valid low-yield data in naturally poor zones, where σ_{local} approaches zero and artificially inflates standard standardizations, hence, a minimum variance floor (σ_{min}) of 0.5 t ha^{-1} was enforced. The localized spatial anomaly was quantified using modified z-score:

$$z = \frac{Y_i - \mu_{local}}{\max(\sigma_{local},\ \sigma_{min})}$$

where Y_i represents the recorded yield at the target point. Data points yielding an absolute z-score of $|z| \geq 2.0$ were flagged as spatial outliers and removed. The resulting cleaned yield data was used for all subsequent analyses.

In this study, the application maps were used (i) to assign VRNF and URNF treatments to the delineated MZs, and (ii) to delineate treatments for extracting treatment-specific yield data (as a mask layer) for subsequent cost-benefit analysis. The application maps were also used to visualize spatial patterns in the site-specific figures (Section 3.2). After cleaning, site-specific yield data were interpolated to a raster and clipped using treatment (multi-)polygons from the application map; the clipped raster layers were then converted into point layers to obtain the mean yield for each treatment (see Appendix D). All processing steps were performed in ArcGIS Pro (v3.4.5). These treatment-level mean yields were used for the cost-benefit analysis presented in Section 3.4. Here, to accurately evaluate the performance of the VR treatments, field-level metrics (treatment specific yield, N-rate, and area) were calculated using area-weighted averages rather than simple arithmetic means. The aggregated treatment specific yield (Y_{VR}) and N application rate (N_{VR}) for the total VR treatment were derived by weighing the observed value in each sub-zone (i) by its specific surface area (A_i):

$$X_{VR} = \frac{\sum_{i=1}^{n}(X_i * A_i)}{A_{total}}$$

where X_{VR} is the weighted average value of yield (t ha^{-1}) or N-rate (L ha^{-1}); X_i is the observed value in specific zone i; A_i is the area of the zone i (ha); A_{total} is the total area of the VR treatment (ha).

For cost-benefit analysis, the gross margin (EUR ha^{-1}) for each treatment was calculated as:

$$\textit{Gross margin} = (\textit{Yield} * \textit{winter barley price}) - \textit{fertilizer input cost}$$

Winter barley price was set at 192 EUR t^{-1}, based on 2025 market estimates for the Odena region provided by the collaborating farmer. Fertilizer costs were calculated from the applied volume of commercial product (Nitro Azufre 32) and its unit price of 0.27 EUR L^{-1} of product. It is worth noting that all other costs such as soil analysis, sensing, land preparation, herbicide, harvesting, and operational costs were assumed to be consistent for all treatments.

2.8. Spatio-temporal variability mapping and crop growth monitoring

S1 and S2 data covering the study site were retrieved from the Copernicus archive for the 2024–2025 winter barley season. Because SAR backscatter is unaffected by cloud cover, the full S1 archive was retrieved, whereas S2 retrieval was restricted to scenes without substantial cloud or cloud shadow. Therefore, reported S2 counts reflect cloud-free availability rather than archive completeness. Both series were subsequently screened for scene quality. Optical scenes showing predominantly bare soil were excluded, and scenes of either sensor whose clipped extent did not fully cover the field boundary were removed (Fig. 6). At the study site (~41°N), 134 S2 acquisitions were retained for time-series monitoring over the 2024–2025 season (January 2024 – July 2025), of which 20 fell within the vigour-onset to senescence clustering window (3rd of February – 21st of May 2025, 108 days), a mean interval of 5.4 days. Eight of these were discarded after visual inspection for cloud or cloud shadow, leaving 12 scenes for clustering (Fig. 6). Scenes acquired after senescence onset (21stof May 2025) were excluded from clustering by design rather than through cloud loss, as progressive canopy yellowing renders most vegetation indices (NDVI, enhanced vegetation index [EVI], green normalised difference vegetation index [GNDVI] and related) insensitive to crop spatial variability once chlorophyll degradation dominates the spectral signal. Post-senescence acquisitions were retained in the time-series monitoring dataset.

Unlike passive optical sensors, C-band SAR backscatter is unaffected by cloud cover, cloud shadow, or solar illumination, so no cloud-based exclusions were required for the S1 series, in contrast to the weather-dependent S2 dataset. SAR backscatter also continues to respond to crop structural and soil properties through senescence and post-harvest stages, where optical vegetation indices become insensitive as chlorophyll degrades. The S1 clustering window at this site therefore extended beyond the S2 senescence cutoff to harvest (3 February – 13 June 2025), including three acquisitions after 21st of May 2025, two of which entered clustering (Fig. 6). Ascending and descending tracks together provided 23 acquisitions over the monitoring period (14th of November 2024 – 6th of July 2025), a mean interval of 10.7 days, including seven consecutive one-day pairs from overlapping tracks. Of the 11

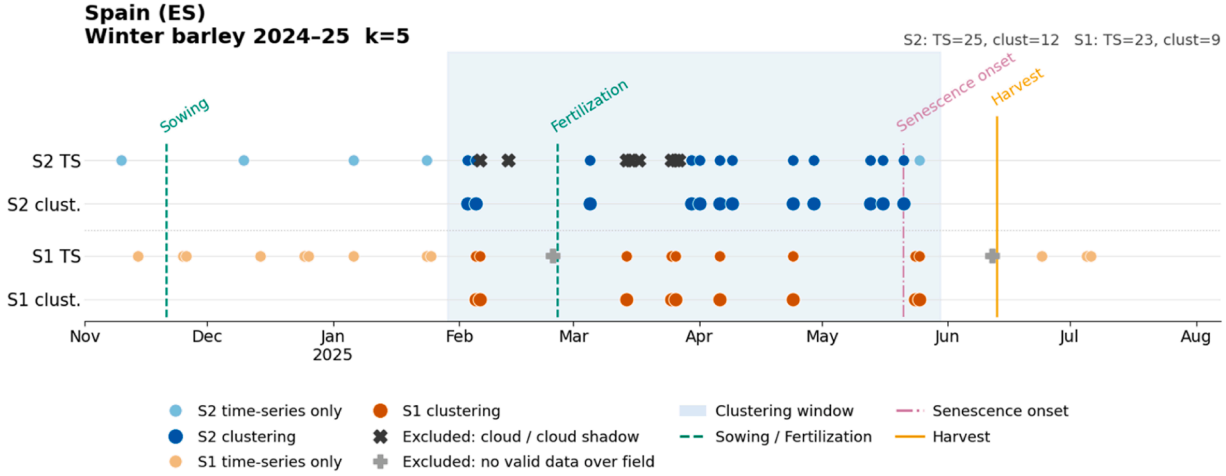


Fig. 6. Temporal distribution of Sentinel-2 (S2) and Sentinel-1 (S1) acquisition dates at the study sites with winter barley, for 2024–2025 season. Saturated markers denote scenes used for k-means clustering; pale markers denote those retained for time-series monitoring only. Crosses mark in-window exclusions: black for S2 cloud or cloud shadow, grey for S1 scenes with no valid pixels over the field. The shaded band spans the clustering window; vertical lines denote key agronomic events.

acquisitions within the clustering window, 9 were used, while 2 returned no valid pixels after clipping to the field boundary and were therefore excluded, the field falling outside the valid data extent of those swaths. These data served two purposes: (i) to derive spatio-temporal variability maps for comparison with soil heterogeneity (from PSS-derived MZD), soil texture, and yield data; and (ii) to identify the indices and metrics most sensitive to crop-growth variability under VRNF and URNF treatments through time-series monitoring.

For each S1 metric and S2 index, all fully covering scenes were stacked chronologically into a time × height × width cube and reshaped to a pixel × time matrix, each row being a pixel's temporal trajectory. Gaps from masking or edge-clipping were filled with the pixel's temporal mean, and pixels outside the field were excluded [34]. Trajectories were z-standardised (zero mean, unit variance) and clustered by k-means (fixed random seed). Cluster labels were ordered by their temporal-centroid means and mapped back to raster geometry, yielding spatio-temporal zone that reflect intra-annual radar and optical dynamics. K-means cluster counts were constrained to five to align with the PSS-derived MZD (Section 3.3), facilitating a direct comparison with static, nutrient-based delineations. Clusters occupying < 0.1% of a field were merged with their nearest neighbour in feature space to suppress "salt-and-pepper" noise.

Treatment-specific time series were extracted by zonal statistics over the URNF and (grouped) VRNF (VRNF-RHS and VRNF-KS) application polygons (via PM); no-data pixels were discarded. At each acquisition, the within-treatment pixel population was summarised by its spatial mean and interquartile range (IQR), and a centred 3-observation moving average was applied to suppress transient noise. Analyses were performed in Python 3.10.

2.8.1. Optical remote sensing

The S2 Multispectral Instrument (MSI) Level-2A surface products provide atmospherically corrected, orthorectified bottom-of-atmosphere (BOA) reflectance [35], suitable for multi-temporal comparison. The S2 bands used in this study are listed in Table 3.

For each retained date, surface-reflectance-based spectral indices were computed from the clipped images to the study area extend (Table 4).

2.8.2. S1 data

Consistent with the S2 sampling period, C-band SAR data (~5.4 cm wavelength) were acquired from Sentinel-1A platform. Following the permanent decommissioning of Sentinel-1B in December 2021 due to an irrecoverable power supply anomaly, the study transitioned to a single-platform acquisition strategy for the latter portion of the analysis. Data were sourced as Interferometric Wide Swath (IWS) dual-polarization ground-range products (VV, VH) from ascending orbits. These were processed to Radiometrically Terrain-Corrected (RTC) backscatter in gamma-naught (γ^0) using the Alaska Satellite Facility HyP3 service [49], with the local incidence angle (LIA) band retained. Within the HyP3 pipeline, spatial speckle filtering (enhanced Lee filter) was applied directly to the linear power data; this preserves radiometric means while suppressing high-frequency noise and avoids the bias associated with filtering directly in logarithmic (dB) scale [50]. Furthermore, HyP3-generated layover and shadow masks were applied to exclude unreliable pixels, water bodies, and no-data areas to ensure the accuracy of the radar backscatter analysis in the full image (https://hyp3-docs.asf.alaska.edu/guides/rtc_product_guide/). After, the acquired output data were geo-coded to UTM/WGS84, co-registered to the S2 grid, and clipped to the field boundaries to ensure a common spatial support (10 m). Since the S1 images were natively speckle-filtered by the provider, redundant local spatial filtering was strictly avoided to prevent the over-smoothing of spatial boundaries. From the filtered linear γ^0 images, comprehensive per-scene SAR metrics were derived and subsequently converted to decibels (dB), yielding: VV (dB), VH (dB), and the cross-polar ratio expressed as 10 $\log_{10}$(VH/VV).

Table 3
Sentinel-2 (Level-2A) bands used in this study.

Sentinel-2 bands	Central wavelength (nm)	Resolution
Band 2 – Blue	492.4 nm (S2-A), 492.1 nm (S2-B)	10m
Band 3 – Green	559.8 nm (S2-A), 559.0 nm (S2-B)	10m
Band 4 – Red	664.6 nm (S2-A), 665.0 nm (S2-B)	10m
Band 5 – RE 1	704.1 nm (S2-A), 703.8 nm (S2-B)	20m
Band 8 – NIR	832.8 nm (S2-A), 833.0 nm (S2-B)	10m
Band 8A – RE 4	864.7 nm (S2-A), 864.0 nm (S2-B)	20m
Band 11 – SWIR	1613.7 nm (S2-A), 1610.4 nm (S2-B)	20m

nm, nanometres; RE, red edge; NIR, near-infrared; SWIR, short wave infrared.

2.8.3. Map concordance and error partitioning

To evaluate spatial agreement between the satellite-derived clusters and the baseline MZD, we applied the cross-tabulation framework of Pontius & Millones [21], which avoids traditional indices (e.g., Kappa) that conflate error sources. Instead, total map disagreement is partitioned into Quantity Disagreement (QD) and Allocation Disagreement (AD), which distinguish differences in class proportions from spatial misplacement. For each comparison, the baseline layer (i.e., site-specific PSS-derived MZD, soil texture, or yield) and the satellite-derived cluster map (S1 or S2) were spatially intersected over valid pixels to generate a cross-tabulation (contingency) matrix of class overlaps. Since unsupervised clustering assigns arbitrary labels, clusters were relabelled in ascending order of their centroid mean prior to cross-tabulation, so that class indices correspond across maps. Cell counts were converted to area (population) proportions p_{ij}, where each element represents the proportion of the study area assigned to reference class i and predicted class j. Row total $r_i = \sum_j p_{ij}$ represents reference class proportions and column totals $c_j = \sum_i p_{ij}$ represents predicted class proportions. From this proportion matrix, agreement and disagreement were computed as follows [21]:

$$\text{Overall agreement } (\text{OA}) = \sum_i p_{ii} \tag{1}$$

the proportion of area where predicted clusters match the baseline layer (i.e., site-specific PSS-derived MZD, soil texture, or yield).

$$\text{Quantity disagreement } (QD) = \frac{1}{2}\sum_i |r_i - c_i| \tag{2}$$

capturing disagreement due to differences in the overall proportions of the mapped clusters, irrespective of spatial location.

$$\text{Allocation disagreement } (AD) = \frac{1}{2}\sum_i 2\min(r_i - p_{ii},\ c_i - p_{tii}) \tag{3}$$

representing disagreement due to spatial mislocation (boundary shifts) after accounting for quantity effects. By construction, OA + QD + AD = 1.

To support interpretation, agreement between each baseline and cluster map was summarised as stacked bar charts showing the per-cluster components of OA, QD, and AD. This decomposition indicates whether divergence from the baseline layer (site-specific PSS-derived MZD, soil texture, or yield) arises primarily from differences in mapped class proportions (quantity) or from spatial displacement of boundaries (allocation).

2.9. Data analyses

Treatment effects on yield were assessed using parametric tests appropriate to the sample structure, and a one-way analysis of variance (ANOVA) was applied. The experimental unit was the sub-polygon: pixel-level yield values (t ha^{-1}) within each sub-polygon were summarized as a mean, and these sub-polygon means served observations were

Table 4
Sentinel-2-derived spectral indices used in this study and their common precision agriculture (PA) applications are summarized from Sishodia et al. [36]. For normalized difference moisture index (NDMI) and moisture stress index (MSI), recent PA and general agricultural application examples are included.

Index symbol	Description and key references	Formula	Applications
NDVI	Normalized difference vegetation index [37]	$\frac{Band\ 8 - Band\ 4}{Band\ 8 + Band\ 4}$	Biomass, breeding, phenotyping, yield, disease, N-management, soil moisture, water stress
NDRE	Normalized difference red-edge index [38]	$\frac{Band\ 8 - Band\ 5}{Band\ 8 + Band\ 5}$	Crop yield and biomass, N-management, disease
EVI	Enhanced vegetation index [39]	$2.5 \times \frac{Band\ 8 - Band\ 4}{Band\ 8 + 6 \times Band\ 4 - \ 7.5 \times Band\ 2 + 1}$	Disease, biomass
GNDVI	Green normalized difference vegetation index [40]	$\frac{Band\ 8 - Band\ 3}{Band\ 8 + Band\ 3}$	Water stress, yield, biomass, disease
SAVI	Soil-adjusted vegetation index [41]	$1.428 \times \frac{Band\ 8 - Band\ 4}{Band\ 8 + Band\ 4 + 0.428}$	Yield, biomass, disease, N-concentration and uptake, water stress
NDMI	Normalized difference moisture index ([42]b)	$\frac{Band\ 8 - Band\ 11}{Band\ 8 + Band\ 11}$	Soil moisture [43], vegetation water content [44]
MSI	Moisture stress index [45]	$\frac{Band\ 11}{Band\ 8}$	Canopy and soil moisture [46,47], drought monitoring [48]

of n = 7, 16 and 18 for UR, VRNF-KS, and VRNF-RHS, respectively, with total n = 41). VRNF-KS and VRNF-RHS each comprised multiple dose-rate sub-classes (L, M, ML, MH, H) that were pooled by prescription strategy, as the comparisons of interest was between strategies rather than individual dose levels. Homogeneity of variances was assessed using Levene's test (centre = median), and Tukey's honestly significant difference (HSD) test was used to account for multiple testing across treatment groups. Statistical significance was defined as $p < 0.05$, with ns, *, **, and *** indicating $p \geq 0.05$, $p < 0.05$, $p < 0.01$, and $p < 0.001$, respectively.

Time-series treatment separability between VRNF and URNF fertilisation was assessed per spectral layer and phenological stage (Appendix C). For each layer-stage combination, the Jeffries-Matusita (JM) distance was computed between VRNF and URNF strip-level medians to quantify distributional separability (range = 0–2), and the dispersion ratio SD_{VRNF}/SD_{URNF} was calculated to characterise the relative spread of the two treatments. Differences in central tendency were tested using the non-parametric Mann-Whitney U test, adopted because the strip-level medians were not normally distributed with significance was set at $p < 0.05$. Combinations with fewer than three strip medians per treatment were excluded. All data analyses were performed in Python (v3.10). Full statistical results are reported in Appendix C (JM distances, panel a; dispersion ratios, panel b).

3. Results

3.1. Accuracy of vis-NIR spectral modelling of soil properties

Across the study areas (i.e., Field-1, Field-2 and Field-3), the summary statistics indicate site-specific soil conditions and generally strong agreement between laboratory measurements and on-line sensor estimates (see Appendix A). In Field-1 (n = 13; 1.26 ha), the largest relative deviation within predicted soil properties was observed for available P_{AL} (i.e., measured mean value of 4.62 mg kg^{-1} vs. the on-line predicted mean value of 6.95 mg kg^{-1}), where the on-line estimates were higher and showed a narrower range. This suggests either a systematic offset in the P_{AL} calibration (via PLSR) or that the denser on-line sampling captured more P-rich microsites that were under-represented with 13 sampling points. SOC, MC and pH were very similar between methods, and both datasets indicate a moderately alkaline soil. Similarly, in Field-2 (n = 101; 10.51 ha), where sampling density was the highest, correspondence between measured and on-line predicted methods was again strong, as on-line predicted means for TN, P_{AL}, SOC, MC, K_{ex}, Mg_{ex}, Na_{ex}, CEC_B and Ca_{ex} were representative of the laboratory standard deviation (SD), similar coefficient of variation (CV), skewness and kurtosis. Meanwhile, Field-3 (n = 24; 2.53 ha) was characterised only from laboratory measured samples because the steep slope imposed mechanical constraints that precluded reliable on-line scanned spectra. Relative to Field-1 and Field-2, Field-3 exhibited an intermediate fertility status. Also, in Field-3, TN and SOC were slightly lower than in Field-2, P_{AL} is comparable to Field-1, and the broader range in K_{ex} (i.e., highest SD and CV) indicate greater within-field heterogeneity on this strongly clayey slope (i.e., clay ~45.2% ±5.0; sand ~16.1% ±6.7; silt ~38.6% ±1.9; Table 1).

3.2. Site-specific yield and spatial variation of soil physical properties

The site-specific yield map and the maps of BD (g cm^{-3}) and soil texture (sand, silt, clay, %) were analysed together with the assigned VRNF treatments (KS and RHS; Fig. 7). The densely sampled BD map (n = 75) revealed clear within-field heterogeneity in compaction across all selected fields (Section B: A-G, Fig. 7). However, zones with higher BD (e.g. B.3 and B.5) did not systematically correspond to low-yield areas. Only some locations with elevated BD (B.2, B.4, B.6, and parts of B.1) coincided with lower-yield zones (sections A and B, Fig. 7), indicating that BD alone did not consistently explain and/or influence yield variation. Similarly, localized extremes in sand, silt, or clay content were not consistently associated with yield gains or losses (C.1-C.3, D.1-D.3, and E.1-E.3). However, because soil texture was mapped from only 13 samples, this low sampling density may have underrepresented within-field spatial variability. Nevertheless, further statistical analysis is required to assess the spatial alignment between soil physical properties (i.e., sand, silt, clay), yield and the optical (S2) and radar (S1) spatio-temporal patterns.

3.3. Spatio-temporal mapping

A subtle "field-edge" effect was consistent when the S2 spatio-temporal data were clustered to match the PSS-derived MZD: 2–3 clusters dominated each parcel, with the remainder(s) corresponding to field edges (Fig. 8). After clustering, all crop-vigour optical indices produced near-identical spatio-temporal patterns, as did the moisture indices (MSI, NDMI) in inverse terms. With the exception of the VV (dB) metric, spatio-temporal clustering of S1 metrics yielded more heterogeneous spatial patterns.

To quantify these relationships, the OA between satellite-derived zones and the reference partitions was computed across all refernce layers (i.e., PSS-derived MZD, yield, soil texture, versus S2/S1 spatio-temporal patterns). OA was consistently low, with no combination exceeding 34% (Figs. 9 and 10). Optical (S2) indices outperformed radar (S1) metrics overall: S2 agreement averaged 26.1% (range 16.9–33.7%), compared with 17.5% (range 11.1–22.3%) for S1. For the S2 indices,

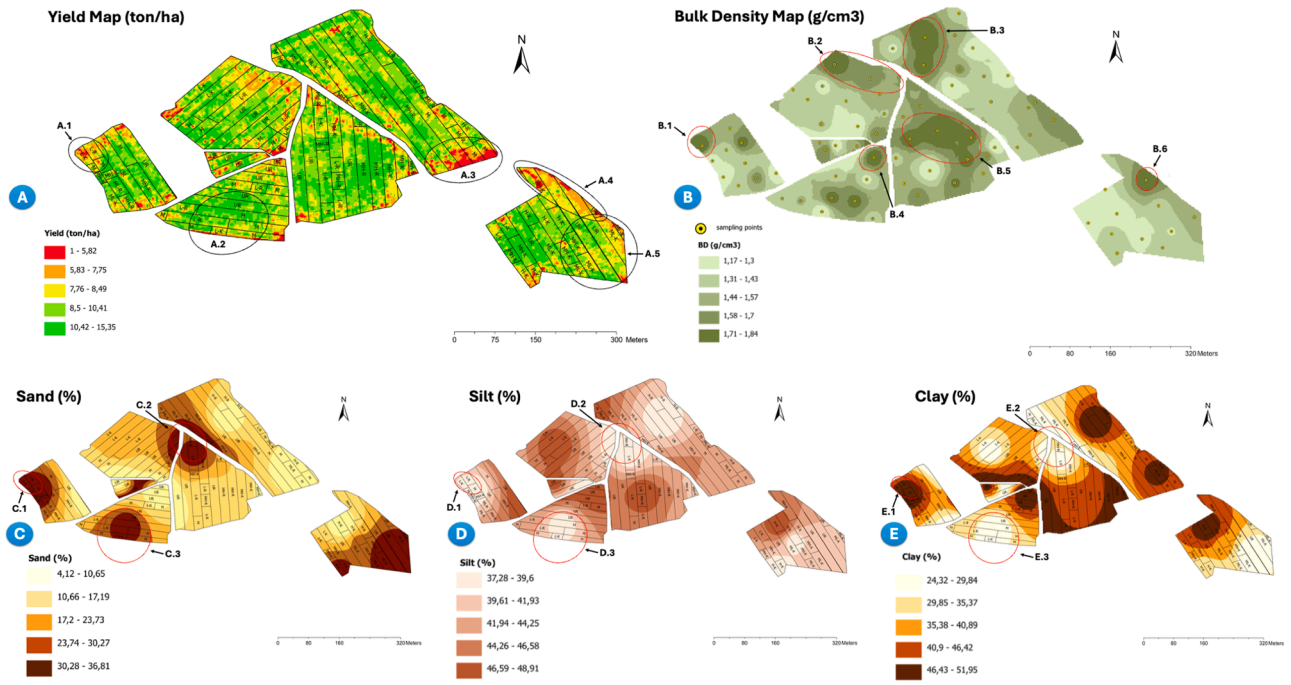


Fig. 7. A. Measured barley yield map (from combine harvester with yield sensor), C., D. and E soil texture maps (sand, silt, clay, respectively, from 13 sampling points collected on 9th of October 2024 and subsequently analysed at the Soil Service of Belgium (BDB, Heverlee, Belgium), and B. bulk density (BD) map from 75 sampling points collected before fertilization. Black circles (A.1-A.5) and red circles (B.1-B.6, C.1-C.3, D.1-D.3, E.1-E.3) indicate areas of visual emphasis only and do not represent management zones (MZs), experimental units, or sampling strata used in the analyses; they are discussed in detail in Section 3.2. For interpretation of the references to color in this figure legend, the reader is referred to the web version of this article.

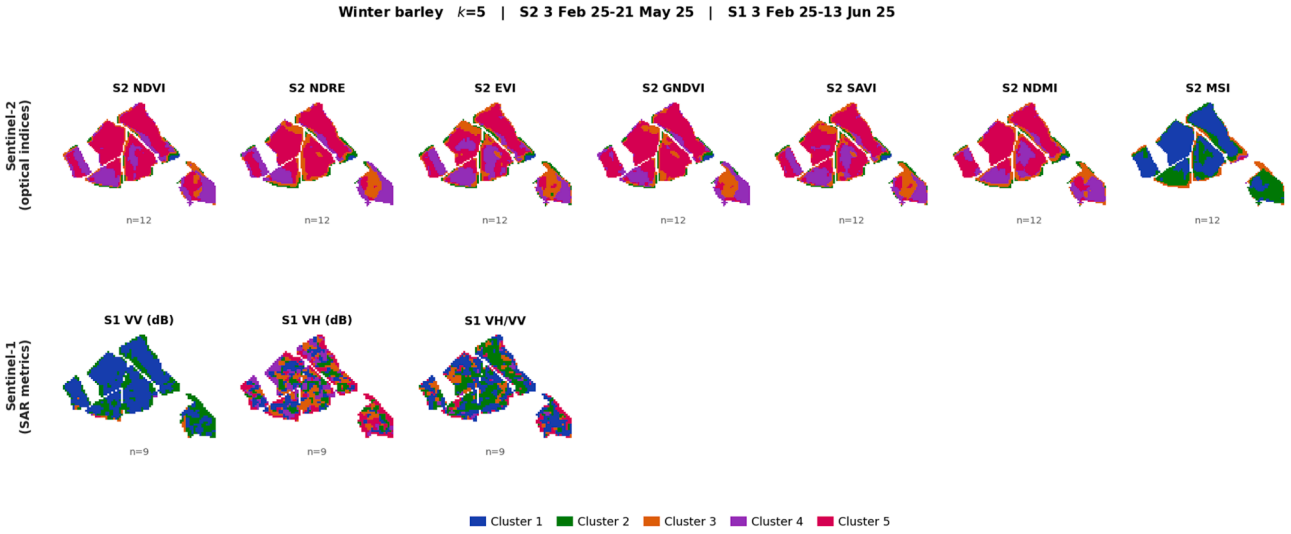


Fig. 8. Spatio-temporal k-means cluster maps derived from Sentinel-2 (S2, top maps) multispectral (NDVI, normalized difference vegetation index; NDRE, normalized difference red-edge index; EVI, enhanced vegetation index; GNDVI, green normalized difference vegetation index; SAVI, soil-adjusted vegetation index; NDMI, normalized difference moisture index; MSI, moisture stress index) and Sentinel-1 (S1, bottom maps) SAR (VV (dB), VV backscatter, VH (dB), VH backscatter, VH/VV, VH/VV backscatter ratio) time series ($k = 5$), using the same k as applied for management zone delineation (MZD). S2 clustering was restricted to the active crop growth period: sowing-harvest and vigour onset-senescence for winter barley (3rd of February – 21st of May 2025). S1 clustering used all available scenes for within the study area (3rd of February – 13th of June 2025; vigour onset-harvest). Cluster labels are ordered by ascending mean centroid value; columns represent individual indices and metrics; n denotes the number of scenes used per panel. For interpretation of the references to color in this figure legend, the reader is referred to the web version of this article.

agreement with the MZD reference was highest for EVI (33.2%) and lowest for NDMI (26.4%). Agreement against the soil-texture references was similarly modest, peaking at 33.7% (NDMI vs. clay) and 32.4% (MSI vs. sand), while the yield reference reached at most 30.3% for GNDVI. The disagreement was dominated by the quantity component in the majority of cases (29 of 35 index-reference combinations), indicating that the satellite indices and reference layers more often differed in the proportion of the field assigned to each class than in its spatial arrangement. For the S1 metrics, agreement was lower across all references. The VH/VV ratio gave the highest agreement against the yield (22.3%) and silt (19.4%) references, whereas agreement with MZD was the weakest of any reference (11.1–16.9%). In contrast to the optical

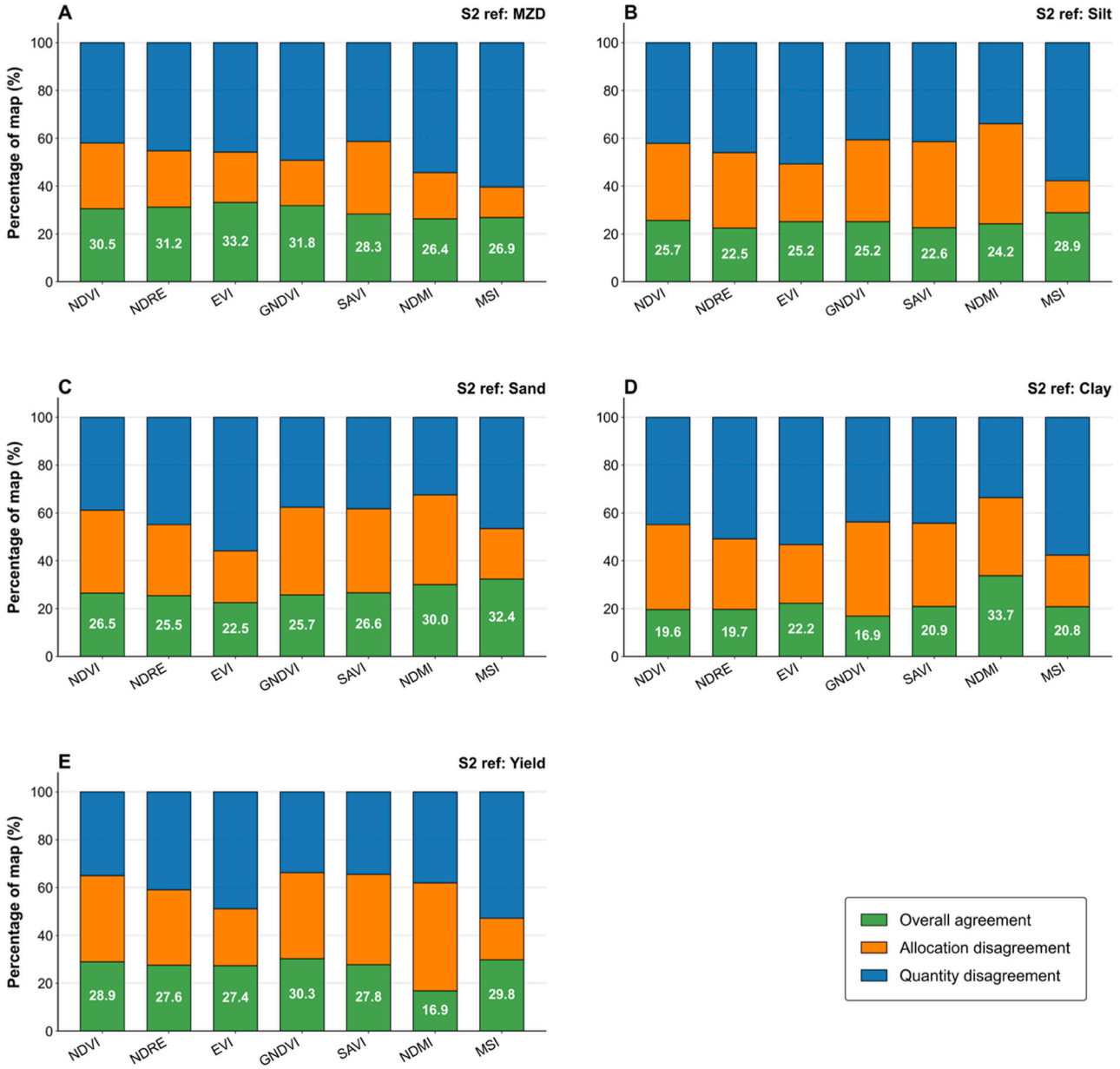


Fig. 9. Spatial cross-consistency analysis [21] between Sentinel-2 (S2) optical index-derived management zones (MZs) and five reference layers (i.e, proximal [on-line] soil sensing delineated MZ, and measured silt, sand, clay, and yield) at the Spanish winter barley sites. Each panel reports the overall agreement (OA, green), allocation disagreement (AD, orange), and quantity disagreement (QD, blue) for seven vegetation indices (i.e., NDVI, normalized difference vegetation index; NDRE, normalized difference red-edge index; EVI, enhanced vegetation index; GNDVI, green normalized difference vegetation index; SAVI, soil-adjusted vegetation index; NDMI, normalized difference moisture index; MSI, moisture stress index). OA values are annotated within each bar. For interpretation of the references to color in this figure legend, the reader is referred to the web version of this article.

indices, S1 disagreement was more evenly split between quantity and allocation components (9 vs. 6 of 15 combinations), reflecting a comparatively larger contribution of spatial misplacement to the total disagreement.

Taken together, these results indicate weak cross-consistency between satellite-derived zones and both soil-texture and yield references within this study, with optical indices showing somewhat closer correspondence than SAR metrics, and QD as the principal source of mismatch, particularly for the optical indices.

3.4. Crop growth monitoring

NDVI remained low through December to January before increasing rapidly from February to peak in late March into early April 2025, consistent with winter barley heading (Fig. 11). GNDVI and NDMI peaked approximately three weeks later, indicating continued canopy water accumulation after greenness had saturated. By senescence onset (21st of May 2025), NDVI had declined substantially and MSI had risen correspondingly, confirming progressive chlorophyll degradation. Although S2 indices tracked greenness and water content, S1 followed a structurally distinct trajectory. VV(dB) declined to its seasonal minimum in March to April 2025, coinciding with maximum canopy volume during tillering and stem extension, then recovered strongly through and beyond senescence, a period when S2 indices had already lost sensitivity; VH(dB) peaked after senescence onset (late May 2025), and VH/VV was highest during active vegetation before declining as surface scattering from desiccated stems came to dominate. Overall, treatment means coincided for both sensors, and no VRNF vs. URNF difference was

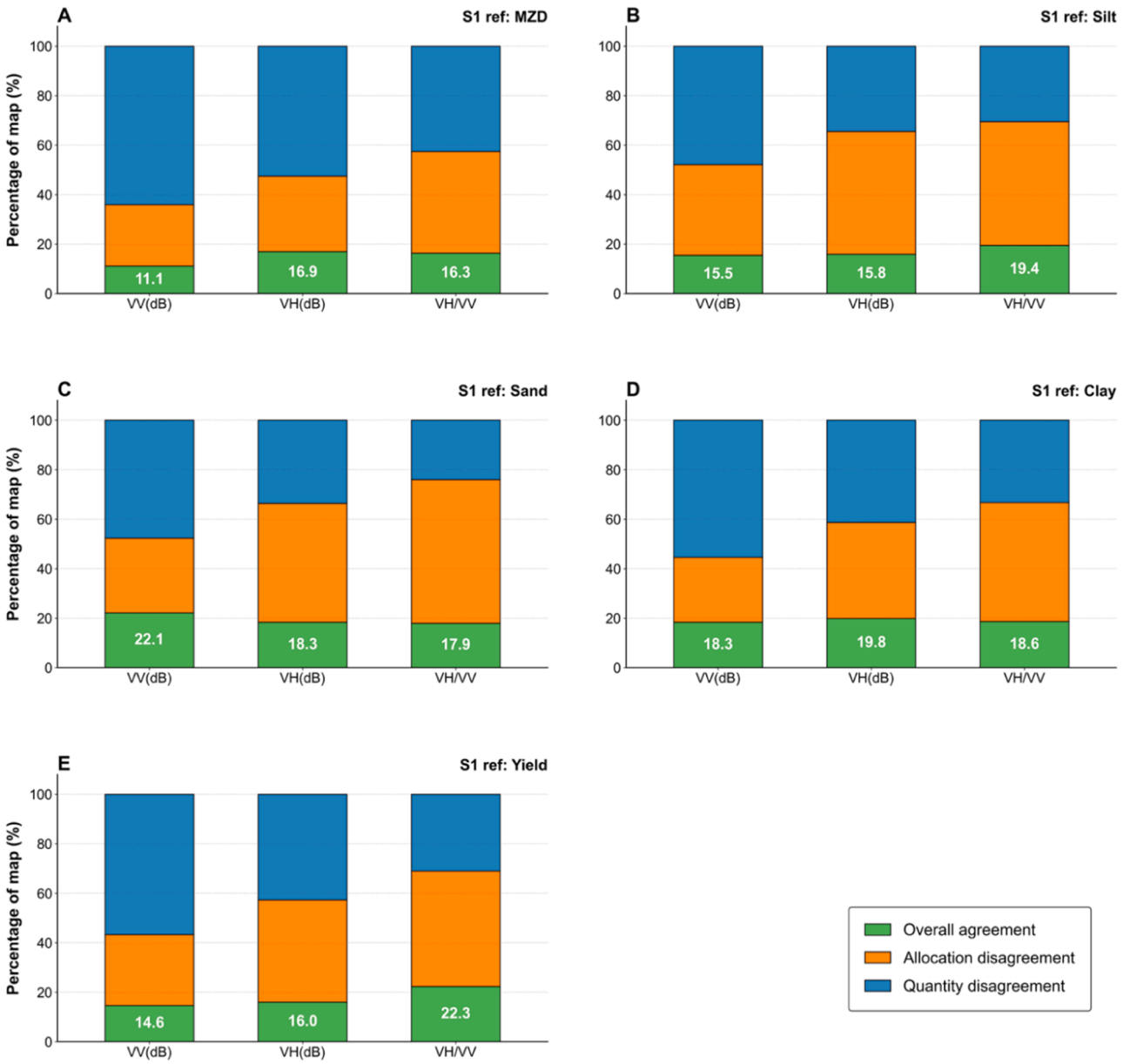


Fig. 10. Spatial cross-consistency [21] between Sentinel-1 Synthetic Aperture Radar (SAR) metric-derived management zones (MZs) and five reference layers (i.e., proximal soil sensing delineated MZ, and measured silt, sand, clay, and yield) at the Spanish winter barley sites. Each panel reports the overall agreement (OA, green), allocation disagreement (AD, orange), and quantity disagreement (QD, blue) for three SAR metrics (VV (dB), VV backscatter, VH (dB), VH backscatter, VH/VV, VH/VV backscatter ratio). OA values are annotated within each bar. For interpretation of the references to color in this figure legend, the reader is referred to the web version of this article.

found to be significant (Mann-Whitney, all $p > 0.05$); separability was instead expressed as dispersion. Markedly higher JM distances (up to 0.84 for VV(dB) at tillering) and 1.8–3.3x greater spread among VR strips were observed for the S1 SAR metrics, particularly for VV(dB) and VH/VV during tillering and stem elongation, whereas all S2 optical indices remained near-identical between treatments (JM $\leq$ 0.07; SD ratio $\approx$ 1.0; see Appendix C). These results indicate that the heterogeneous canopy structures produced by differential N application rates were reflected in greater S1 SAR backscatter dispersion but not in S2 optical vigour indices.

3.5. Economical assessments

The economic and agronomic performance of the two VRNF schemes (VRNF-KS and VRNF-RHS) was benchmarked against the URNF application (Table 6). VRNF-KS showed a slight yield reduction of −0.20 t ha^{-1} and a gross margin loss of −34.54 EUR ha^{-1} relative to URNF, whereas VRNF-RHS achieved a yield gain of +0.21 t ha^{-1} and the highest relative gross margin (+41.15 EUR ha^{-1}). Thus, the two strategies diverged in economic outcome: VRNF-KS delivered a modest N saving but underperformed both URNF and VRNF-RHS in gross margin terms, while VRNF-RHS improved both yield and gross margin relative to the URNF baseline and VRNF-KS while applying marginally less N. While across the VR levels (VR-L to VR-H), yields ranged from 7.17–8.07 t ha^{-1} for winter barley (Appendix D).

Overall, yields were comparable across URNF (7.71 $\pm$ 0.39 t ha^{-1}), VRNF-KS (7.52 $\pm$ 0.53), and VRNF-RHS (7.90 $\pm$ 0.53; $F(2, 38) = 2.280$, $p = 0.116$), with VRNF-KS vs. VRNF-RHS approaching but not reaching significance ($p = 0.096$). However, no significant difference was observed between URNF, VRNF-KS and VRNF-RHS (Fig. 12).

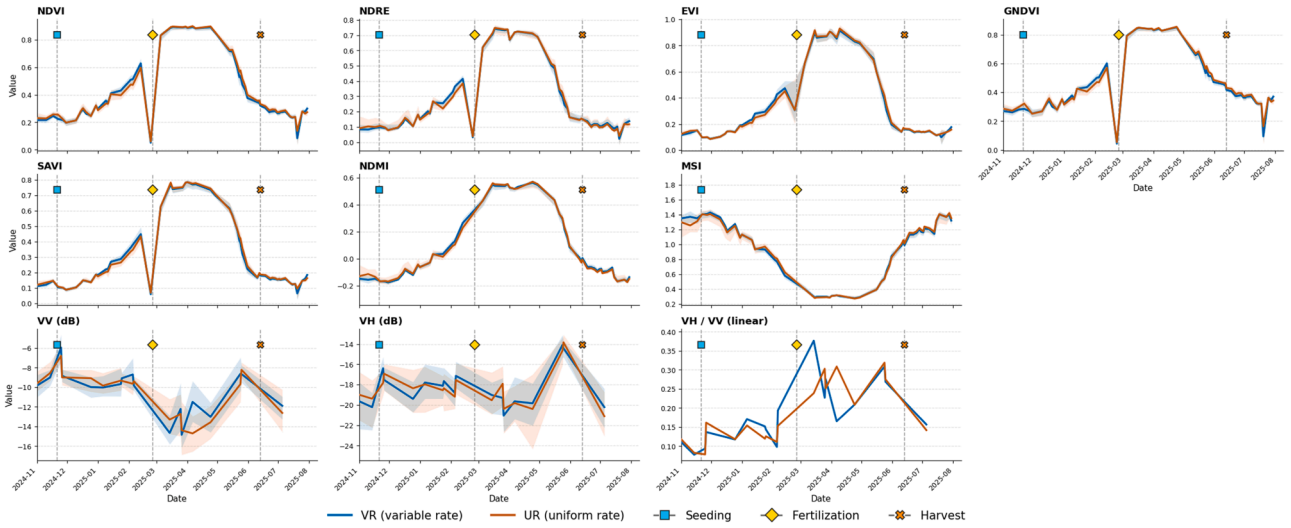


Fig. 11. Time series of Sentinel-2 spectral indices (NDVI, normalized difference vegetation index; NDRE, normalized difference red-edge index; EVI, enhanced vegetation index; GNDVI, green normalized difference vegetation index; SAVI, soil-adjusted vegetation index; NDMI, normalized difference moisture index; MSI, moisture stress index) and Sentinel-1 SAR metrics (VV (dB), VV backscatter, VH (dB), VH backscatter, VH/VV, VH/VV backscatter ratio) for the study site. Lines show the treatment-plot median for each fertilisation regime, variable-rate (VR) and uniform-rate (UR), with shaded bands indicating the interquartile range (Q25-Q75). Vertical dashed lines mark key management activities (seeding, fertilisation, harvest).

Table 6
Cost-benefit and nitrogen (N) use analysis of variable rate nitrogen fertilizer (VRNF) applications under the Robin Hood (RHS) and King's (KS) schemes, compared with uniform rate N fertilisation (URNF) treatment.

Treatment	Area (ha)	N input[a] (kg N ha^{-1})	Commercial fertilizer application rate[b] (L ha^{-1})	Fertilizer input cost[c] (EUR ha^{-1})	Yield[e] (t ha^{-1})	Revenue (EUR ha^{-1})	Gross margin[d] (EUR ha^{-1})	Δ Yield[f] (t ha^{-1})	Δ Gross margin[f] (€ ha^{-1})
URNF	4.56	60	203	54.81	7.72	1482	1428		
Total VRNF-KS	4.88	56	189	51.03	7.52	1444	1393	−0.20	−34.54
Total VRNF-RHS	4.12	59	200	53.98	7.93	1523	1469	0.21	41.15

[a] N input; farmer baseline rate (R) = 60 kg N ha^{-1}. Derived from the commercial fertilizer application rate using the product's N concentration (Section 2.6).
[b] Application rate; values for total VR are area-weighted mean across management zones (MZs).
[c] Fertilizer input cost = application rate * 0.27 EUR L^{-1} of commercial product; see Section 2.7.
[d] Gross margin = Revenue (Yield * crop price) – fertilizer input cost (detailed in Section 2.7). All other costs (e.g., soil analysis, on-line soil sensing, land preparation, herbicide, harvesting, other operations) were assumed equal across treatments.
[e] Zone-level yield data are provided in Appendix D.
[f] Δ = within-field contrast. For three fields total gross margin and yield for VRNF-KS and VRNF-RHS: Δ vs UR = Total VR − UR; positive values indicate the treatment outperforms the reference; negative values indicate underperformance.

4. Discussions

4.1. Site-specific yield and spatial variation of soil physical properties

For soil texture (n = 13), the low sampling density is likely a major limitation. Since topographic factors (i.e., slope, solar radiance) and soil texture affects nutrient or water retention, enzyme activity (a common known proxy for soil health and activity), and water infiltration capacity texture is particularly essential in crop growth in Mediterranean environments [51]. Meanwhile, previous works have shown that the KS and RHS treatments can be both fertilizer-efficient and effective for managing within-field variability in commercial fields, specifically, VRNF and manure applications on 8 to 12 ha commercial fields in the Flanders region (Belgium) [8,11] and VRNF application on a 9 ha field in Albacete (Spain) [52]. In our experiment, only adoption of the VRNF-RHS treatment outperformed the conventional URNF approach, delivering higher yields and improved gross margins (Table 6) relative to applying a single N across spatially heterogeneous soil and topographic conditions. Meanwhile, VRNF-KS neither delivered higher yield or gross margin, but it saved N inputs. In addition, site-specific soil texture and BD maps were used as explanatory factors for the effectiveness of VRNF application through comparative interpretation of site-specific yield maps, rather than relying solely on commonly reported cost-benefit assessments. Accordingly, within the scope of this study, it was observed that VRNF application can at least partly compensate for underlying differences in soil properties such as soil texture and BD, such that areas with higher BD or coarser textures did not directly result in lower yields (Fig. 7). However, this inference is site-specific and should be regarded as indicative, where yield variation can be also influenced by the combined interaction of site-specific factors not assessed in this study, including seasonal rainfall distribution, water stress, topography, spatial soil water-holding capacity, and management history. Consistent with findings by Amangeldy et al. [6], in which yield losses under the VRNF-RHS were attributed to non-N limiting factors across three Nitrate Vulnerable Zone fields, therefore, further studies are needed to determine whether VRNF can consistently buffer the effects of soil texture, BD, topographic variation, and farmer's management history across sites and/or years, and to assess the associated environmental footprints.

Soil sampling and on-line proximal soil sensing costs were not included in the cost-benefit analysis, as all non-fertilizer costs were assumed constant across treatments. However, previous works (e.g., Munnaf et al. [53]) utilising the same on-line multi-sensor platform

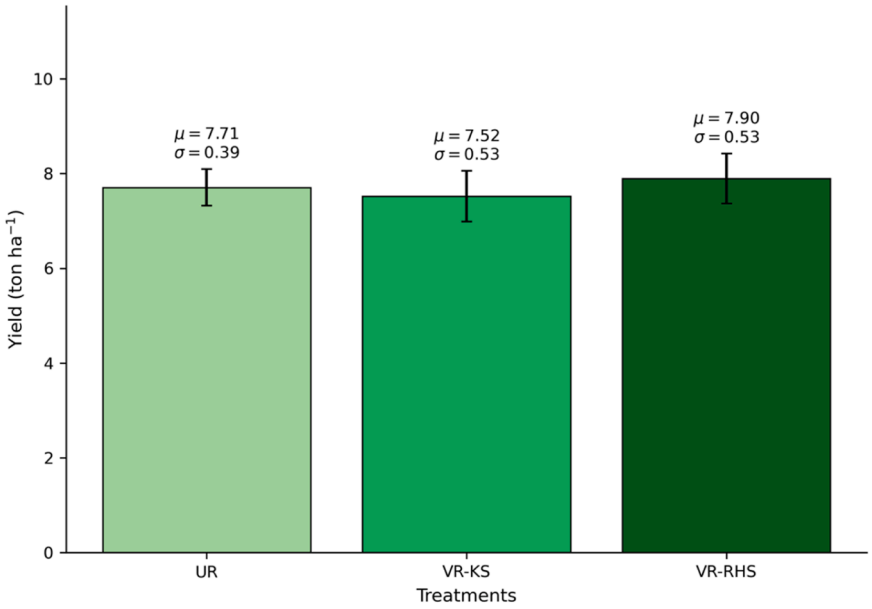


Fig. 12. Yield data collected with yield-sensor-equipped harvester comparing uniform-rate and variable-rate nitrogen (N) fertilization (URNF and VRNF). Two variable-rate schemas were implemented: (i) the Robin Hood approach (VRNF-RHS, higher rates on lower fertility zones and vice versa) and (ii) King's approach (VRNF-KS, lower rates to lower fertility zones and vice versa). The bars represent mean yield values, while the error bars indicate the standard deviation of measurements.

estimated the cost of soil scanning to be 25 EUR ha^{-1}, which can be used not only for VRNF, by also for VR manure application, precision seeding, precision tillage and even for VR phosphorous, potassium and liming applications. This means that for VRNF, we estimate the share of on-line soil scanning cost would be 3–5 EUR ha^{-1}, which if deducted from the gross margins in Table 6, would not change the conclusions we reached neither for VRNF-KS nor for VRNF-RHS. Additionally, the 138 samples collected over 14.3 ha within this study were needed to calibrate and validate the vis-NIR models and to provide a reliable evaluation reference for the VRNF strategy, which does not represent the sampling density required for operational MZD, varying with field size, soil variability, and the sensing approach adopted. In practice, farmers can opt for either (i) intensive spatial soil sampling analysed by traditional laboratory methods, a practice that is costly and time consuming, hence, preventing high sampling density necessary for VRNF implementation or (ii) gradually reduced soil sampling density for traditional laboratory analysis, but then combine with on-line vis-NIR sensing deployed across multiple seasons to reduce costs over time as the spectral library expands. Both approaches were applied across sites in this study, except at Field-3 (c in Fig. 4), where steep topography precluded sensor deployment, and 24 soil samples were used for spatial mapping instead. Implementing PSS therefore (a) overcomes the shortcomings of the traditional soil sampling and laboratory analysis by delivering the high sampling density VRNF requires, while remaining complimentary to – rather than a replacement for – reference measurements, and (b) enables profitable VRNF at a cost of on-line scanning of 25 EUR ha^{-1}, cut down to 3–5 EUR ha^{-1} for VRNF. Comparing this extra cost of on-line scanning to the gross margin of 41 EUR ha^{-1} calculated for the VRNF-RHS (Table 6), about 10% reduction of gross margin is expected. This result is in line with previous studies deploying the on-line multi-sensor scanner for map-based VRNF and manure application [8,11].

4.2. Spatio-temporal mapping and crop growth monitoring

S1 SAR and S2 optical remote sensing and PSS-derived MZs are complementary, not interchangeable (Figs. 9 and 10). The consistently low S2 vs. MZD and S1 vs. MZD agreement (OA < 34% throughout; S2 mean 26.1%, S1 mean 17.5%) indicating canopy reflectance and radar backscatter (both expressing the realised crop condition during the season), capture within-field variability differently from the PSS-derived MZD representing soil fertility levels, which reflects underlying edaphic potential [54–56]. The S2 optical indices agreed marginally better with MZD than the S1 radar metrics did, with four of seven S2 indices reaching 30–33% (EVI = 33.2%, GNDVI = 31.8%, NDRE = 31.2%, NDVI = 30.5%), yet even these represent only weak correspondence. For both sensors, the disagreement against MZD was quantity-dominated (S2: mean QD 48% vs. AD 22%, with QD exceeding AD for every index; S1: mean QD 53% vs AD 32%), indicating that the satellite and soil zonations differed more in the proportion of the field parcels assigned to each class than in where the boundaries fell [21]. Taken together, these results reinforce treating PSS-derived MZD and remote optical and/or radar sensing as complementary layers in zone design rather than substitutes.

The texture and yield references produced low-to-moderate agreement across both sensors, with disagreement distributed across both components: QD was generally the larger term for S2, whereas for S1 the balance shifted to allocation against the coarser silt and sand fractions and back to quantity against clay and yield. The single highest agreement anywhere was NDMI vs. clay (OA = 33.7%), essentially tied with EVI vs. MZD (33.2%). Notably, the NDMI vs. clay agreement combined near-equal quantity and allocation terms (QD = 33.6%, AD = 32.7%), and NDMI vs. silt, although lower overall (OA = 24.2%), carried the largest allocation share of any S2 comparison (AD = 41.8%). In both cases the substantial allocation term indicates partial but genuine spatial co-location rather than a match in class proportions alone, which an OA or Kappa statistic in isolation could mask [21,57]. This correspondence is physically coherent: NDMI is a canopy-moisture index, and the silt and clay fractions govern soil water-holding capacity, so their co-located agreement plausibly reflects a shared moisture control on crop condition rather than a statistical coincidence. The Pontius & Millones [21] decomposition is what makes this distinction visible: by separating quantity from allocation, it shows that even moderate agreement against the soil references carries a real co-located component rather than reducing to a class-proportion effect [21,58].

Consequently, the following sources of variability in cross-consistency outcomes were identified: (i) site-specific soil-property

composition and spatial-variance structure governing MZD configuration (Appendix A); (ii) known factors not included in this study, such as incomplete S2 optical coverage during critical growth stages due to cloud gaps, topographic effects, and/or biotic stress; and (iii) partially characterised factors, such as seasonal weather variability, and farming history. In this context, a further consideration is the cluster number. Although $k = 5$ was fixed to match the MZD, this selection is not optimal for every variable, since each index and metric captures a different component of within-field variation. The constraint applies identically to S1 and S2, however, as neither satellite asset is favoured by the choice, and implementable MZ counts are bounded in any case by VR machinery resolution. Future work should assess how cluster number influences cross-consistency across additional fields and growing seasons, as the present findings derive from a single season at a limited number of sites.

4.3. Economical assessments

Implementing the same approach in barley-wheat systems, Guerrero et al. [8] demonstrated that both strategies, VRNF-RHS and VRNF-KS, built from on-line vis-NIR soil sensing, NDVI and yield data improved gross margin and reduced N surplus compared with URNF application. The most profitable scenario was the one that applied more N towards low-fertility zones and reduced N in high-fertility zones (i.e., VRNF-RHS), while maintaining or increasing yield (up to ~10.4% gain) and lowering total N input by up to ~19.4% relative to URNF, which is conceptually consistent with the performance of the VRNF-RHS in this study, where VRNF-RHS outperformed URNF and VRNF-KS in relative gross margin. Also, VRNF treatments implemented by Tsitouras et al. [59] in durum wheat that adopted UAV/sensor-based VR-N in about 3–4 ha commercial fields (located in Thessaly, central Greece) increased net returns relative to UR-N treatments while reducing environmental N losses (NO_3^-) in at least one of the fields, illustrating that redistributing N within-field can raise profitability in heterogeneous fields. For winter wheat in smallholder systems, Wang et al. [60] showed that VR fertilization based on site-specific MZs reduced N, P and K fertilizer use by about 23–44%, 59–100% and 8–100%, respectively, while maintaining yield and increasing farmers' net income by roughly 15–450 USD ha^{-1} compared with traditional UR fertilization; field-scale economic gains were therefore dominated by input savings and improved NUE rather than large yield increases. In a longer-term assessment of thirteen wheat and seven barley N rate trials on commercial fields (located within the northwest region of Buenos Aires Province, Argentina) between 2017–2019, de Lara et al. [61] showed that the site-specific economic optimum N rate (EONR) varies strongly within fields and between years, and that a single uniform N rate frequently overshoots local EONR, implying unnecessary N cost and environmental load in substantial parts of the field. Their machine learning-based EONR estimation demonstrated that soil and crop factors (particularly soil P and organic matter) drive large within-field variability in optimal N rate.

The gross-margin gains and losses reported in this study reflect a single price scenario for winter barley and N fertiliser, both of which are subject to market fluctuation. In recent work at three Belgian sites, the cost of locally available synthetic fertilisers and of VR technology use also influenced final gross-margin outcomes [6]. The present estimates assume no additional charge for soil analysis, or VR equipment, as the cooperating farmer was already equipped with VR fertilisation technology. Indeed, gain and loss estimates would differ where these costs are incurred. Therefore, the present study, by contrast, covers only a single year and still requires comparative assessment across multiple fields. Nevertheless, its findings are consistent with existing evidence that VRNF-RHS can deliver higher relative gross margins than URNF or VRNF-KS [8,11] by reallocating N and substantially reducing N input while keeping yield close to the URNF baseline. Taken together, although both VRNF treatments may reduce N inputs, the limited scientific reports of GHG emissions and N losses (e.g., leaching, volatilisation) alongside yield responses constrains a full assessment under current sustainability policies [6].

5. Conclusions

In three rainfed winter barley fields totalling 14.3 ha, vis-NIR on-line soil sensing-derived MZs provided a high-resolution basis for site-specific N management under the VRNF-KS and VRNF-RHS schemes. Benchmarked against conventional URNF application, the two VRNF strategies produced contrasting outcomes. VRNF-RHS improved both yield (+0.21 t ha^{-1}) and gross margin (+41.15 EUR ha^{-1} relative to URNF) while applying marginally less N, making it the better-performing strategy from both agronomic and economic perspectives. In contrast, VRNF-KS prioritised input reduction, achieving a modest N saving but incurred a slight yield penalty (−0.20 t ha^{-1}) and a gross-margin loss (−34.54 EUR ha^{-1}) relative to URNF, indicating that reducing N inputs alone did not translate into economic gain under the conditions tested. Yields did not differ significantly among UR, VRNF-KS, and VRNF-RHS ($F(2, 38) = 2.280$, $p = 0.116$), indicating that these economic differences emerged despite statistically comparable yields.

Cross-consistency analysis using the Pontius & Millones [21] framework revealed consistently low agreement between remote-sensing-derived spatio-temporal zones and PSS-derived MZs (overall agreement < 34%), indicating that optical and SAR signals reflecting realised crop condition rather than underlying edaphic potential. The broadband S2 indices differentiated the treatments only weakly and behaved similarly to one another, whereas S1 VH/VV captured treatment-associated canopy structural heterogeneity relatively more distinctly, suggesting that SAR is a potentially more sensitive indicator of VRNF-driven within-field variability. However, this difference based on a single growing season was expressed as greater dispersion rather than a statistically significant separation. S1 also appeared to retain sensitivity later into the season than the S2 indices, although the sparse late-season SAR coverage in this study restricts the strength of that observation.

The interactions between management-zone delineation approach, farm management history, topographic position, and crop N-response functions remain incompletely understood, and their relative contributions to site-dependent VRNF outcomes could not be quantified within the scope of this single-year, single-site study. Future work should evaluate for these factors across sites and growing seasons to test the consistency of these patterns and to improve the predictive power and transferability of satellite-assisted VRNF strategies under diverse European agro-environmental conditions.

Declaration of generative AI and AI-assisted technologies in the manuscript preparation process

During the preparation of this work the author(s) used GPT-4 OpenAI in order to check readability. After using this tool/service, the author(s) reviewed and edited the content as needed and take(s) full responsibility for the content of the publication.

CRediT authorship contribution statement

Nazerke Amangeldy: Writing – original draft, Visualization, Validation, Methodology, Investigation, Formal analysis, Data curation, Conceptualization. **Eduardo A. Garcia-Braga:** Writing – review & editing, Supervision, Methodology, Formal analysis, Data curation, Conceptualization. **Yasmina Chourak:** Writing – review & editing, Methodology, Formal analysis, Data curation, Conceptualization. **Gerard Portal:** Writing – review & editing, Supervision, Methodology, Formal analysis, Data curation, Conceptualization. **Hongzhen Luo:** Writing – review & editing, Methodology, Conceptualization. **Isi Bardají:** Writing – review & editing, Methodology, Conceptualization. **Mercè Vall-llossera:** Writing – review & editing, Methodology,

Conceptualization. **Rosa Vilaplana Ventura:** Writing – review & editing, Supervision, Methodology, Funding acquisition, Conceptualization. **Antonios Morellos:** Writing – review & editing, Methodology, Conceptualization. **Manuel Vázquez-Arellano:** Writing – review & editing, Methodology, Conceptualization. **Erik Meers:** Writing – review & editing, Supervision, Methodology, Funding acquisition, Conceptualization. **Estefania Blanch:** Writing – review & editing, Supervision, Methodology, Funding acquisition, Conceptualization. **Abdul M. Mouazen:** Writing – review & editing, Supervision, Methodology, Funding acquisition, Conceptualization.

Declaration of competing interest

The authors declare that they have no known competing financial interests or personal relationships that could have appeared to influence the work reported in this paper.

Acknowledgments

The authors acknowledge funding received from the European Union under the Horizon Europe program, Grant Agreement No 101060455 (NutriBudget project), the Horizon Europe program Grant and Swiss State Secretariat for Education, Research and Innovation (SERI), Grant Agreement No 101156480 (WHEATWATCHER project), the European Union under the Erasmus+ program, Grant agreement No 101139985 (VTSKILLS project) and Strategic Plan of the CAP 2023–2027, co-financed by the Ministry of Agriculture, Fisheries and Food (MAPA), the European Union, and the Government of Catalonia.

Appendix A

Table A.1
Summary of sampling points used to calibrate partial least squares regression (PLSR) visible and near infrared (vis-NIR) spectral models for soil fertility attributes. The table reports laboratory measurements of soil samples collected within each field, which was subdivided into three sub-fields (Table 1) to minimise gaps in sampling coverage and improve geostatistical analysis.

Soil properties	Measured samples							Number of samples (n)	On-line measurements								
	mean	sd	min	max	CV (%)	Skewness	Kurtosis		mean	sd	min	max	CV (%)	Skewness	Kurtosis	RPD	RPIQ
Field-1 (n = 13)																	
TN	140.31	20.93	104	168	0.15	−0.20	−1.06	96	141.28	11.39	100.07	168.92	0.08	−0.53	0.71	4.32	4.61
P_{AL}	4.62	1.55	3	8	0.31	0.48	−0.55	99	6.95	1.28	3.22	9.97	0.18	−0.22	−0.14	2.01	3.37
SOC	1.64	0.37	1.16	2.60	0.23	1.44	2.94	109	1.66	0.19	1.10	2.14	0.11	0.05	−0.49	3.11	3.81
MC	15.29	1.98	11.02	17.62	0.13	−0.52	0.03	101	15.46	0.95	12.64	17.99	0.06	0.37	−0.17	2.24	2.90
K_{ex}	41.31	8.35	31	58	0.20	0.30	−0.52	100	43.33	6.11	27.68	60.62	0.14	0.31	−0.17	2.56	2.61
Mg_{ex}	109.54	7.99	94	122	0.07	−0.24	0.30	111	111.20	4.56	96.67	125.94	0.04	0.21	0.04	2.04	2.36
Na_{ex}	8.88	0.96	6.90	11	0.11	0.19	1.96	102	9.50	0.81	6.84	12.74	0.09	0.30	−0.15	1.70	2.75
Ca_{ex}	12,415.38	380.45	11,600	12,900	0.03	−1.00	0.55	94	12,456	205.72	11,930	13,148	0.02	0.52	0.33	2.45	3.93
CEC_B	631.34	19.44	589.46	656.70	0.03	−0.97	0.57	83	634.71	8.40	614.60	659.63	0.01	0.37	0.19	2.80	3.00
$pH_{(KCl)}$	7.89	0.08	7.80	8.00	0.01	0.00	−0.62										
Field-2 (n = 101)																	
TN	160.22	25.85	93	213	0.16	−0.36	−0.14	101	165.70	24.05	85	220.97	0.15	0.04	−0.47	2.21	2.38
P_{AL}	10.85	3.97	3	22	0.36	0.58	0.40	105	11.96	4.31	3	23.98	0.36	0.51	−0.09	2.73	2.85
SOC	1.81	0.47	0.68	3.60	0.26	1.26	3.09	110	1.99	0.64	0.50	3.70	0.32	0.33	−0.23	2.14	2.86
MC	18.40	1.94	13.24	22.63	0.11	0.01	−0.24	104	18.37	2.40	10.07	24.97	0.13	−0.03	0.54	2.07	3.38
K_{ex}	58.78	15.25	16	99	0.26	0.14	−0.07	105	60.13	18.10	27	101.99	0.30	0.48	−0.51	2.67	3.64
Mg_{ex}	110.39	12.57	91	161	0.11	1.29	2.53	104	113.73	12.55	87.03	161.30	0.11	0.43	−0.14	2.08	1.19
Na_{ex}	8.01	1.37	5.60	14	0.17	1.29	2.53	103	8.13	1.36	4	15.29	0.17	0.30	0.47	1.53	1.97
Ca_{ex}	11,508.91	548.47	9600	12,700	0.05	−0.44	1.48	99	11,567.50	517.69	9398.45	12,899.96	0.04	−0.14	0.31	2.01	2.78
CEC_B	586.50	27.43	489.47	646.56	0.05	−0.44	1.65	105	587.62	30.94	460.73	679.78	0.05	−0.33	0.58	3.15	4.10
$pH_{(KCl)}$	7.91	0.09	7.70	8.10	0.01	0.16	−0.03										
Field-3 (n = 24)																	
TN	134.50	39.37	44	211	0.29	−0.58	0.72										
P_{AL}	10.67	5.36	4	25	0.50	0.80	0.66										
SOC	1.63	0.72	0.	4	0.44	1.02	1.59										
MC	18.09	2.05	14	21	0.11	−0.63	−0.10										
K_{ex}	47.88	13.72	18	81	0.29	0.06	1.69										
Mg_{ex}	115.46	7.35	103	129	0.06	−0.07	−0.59										
Na_{ex}	8.16	1.11	7	11	0.14	0.87	0.44										
Ca_{ex}	11,070.83	415.44	9900	11,700	0.04	−0.75	1.69										
CEC_B	564.75	20.75	507	596	0.04	−0.72	1.64										
$pH_{(KCl)}$	7.95	0.11	7.8	8.2	0.01	0.70	1.21										

n, indicates the number of sampling locations and/or data points included in the PLSR spectral library; sd, standard deviation; mean, average values of sampling points and/or vis-NIR predicted properties; min, minimum of sampling points and/or vis-NIR predicted properties; SOC, soil organic carbon (%); P_{AL}, plant available-phosphorus (mg/100 g soil); K_{ex}, potassium (mg/100 g soil); Mg_{ex}, magnesium (mg/100 g soil); MC, moisture content (%); CEC_B, cation exchange capacity by bases (mg/100 g soil); TN, total nitrogen; CV, coefficient of variation; RPD is residual prediction deviation; RPIQ, performance to interquartile distance. Prediction accuracy was classified based on RPIQ values as excellent (RPIQ > 2.5), very good (2.0–2.5), good (1.7–2.0), fair (1.4–1.7), and poor (RPIQ < 1.4) [32].

Appendix B

Fig. B.1, two-stage outlier detection in barley crop yield mapping.

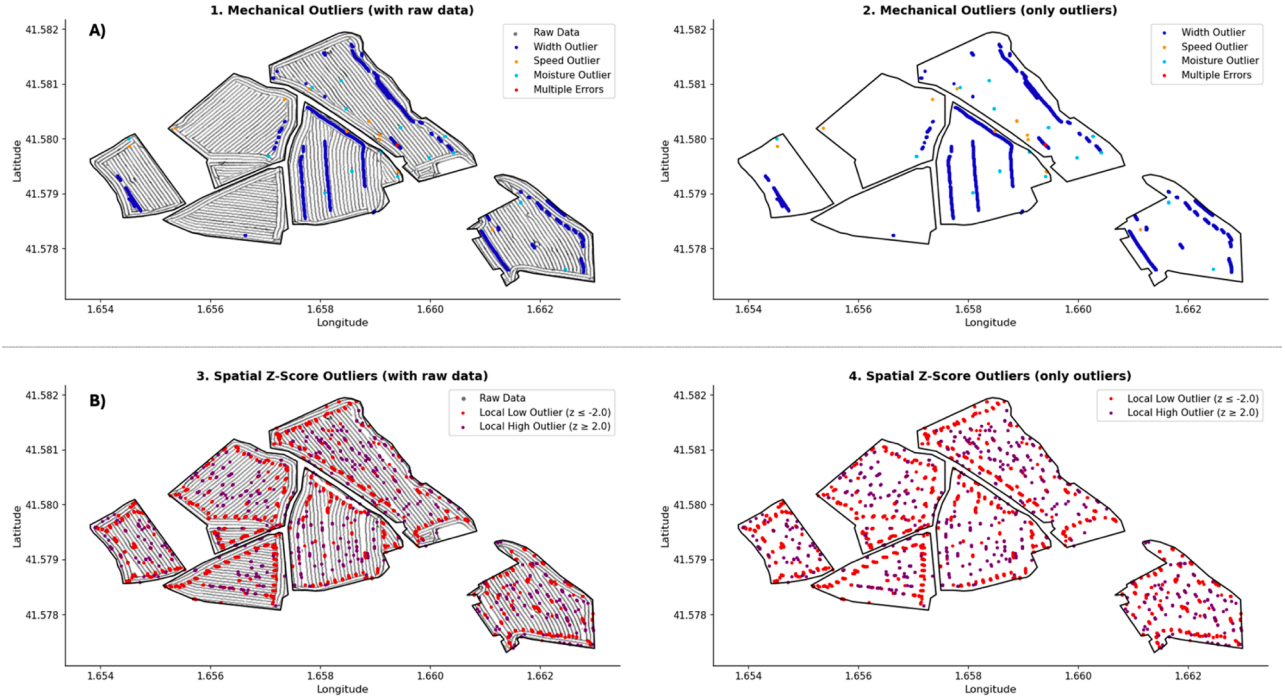


Fig. B.1. Two-stage outlier detection in barley crop yield mapping, showing isolated outlier points removed via harvester mechanical limits (A) and local moving-window spatial z-scores (B).

Appendix C

Fig. C.1.

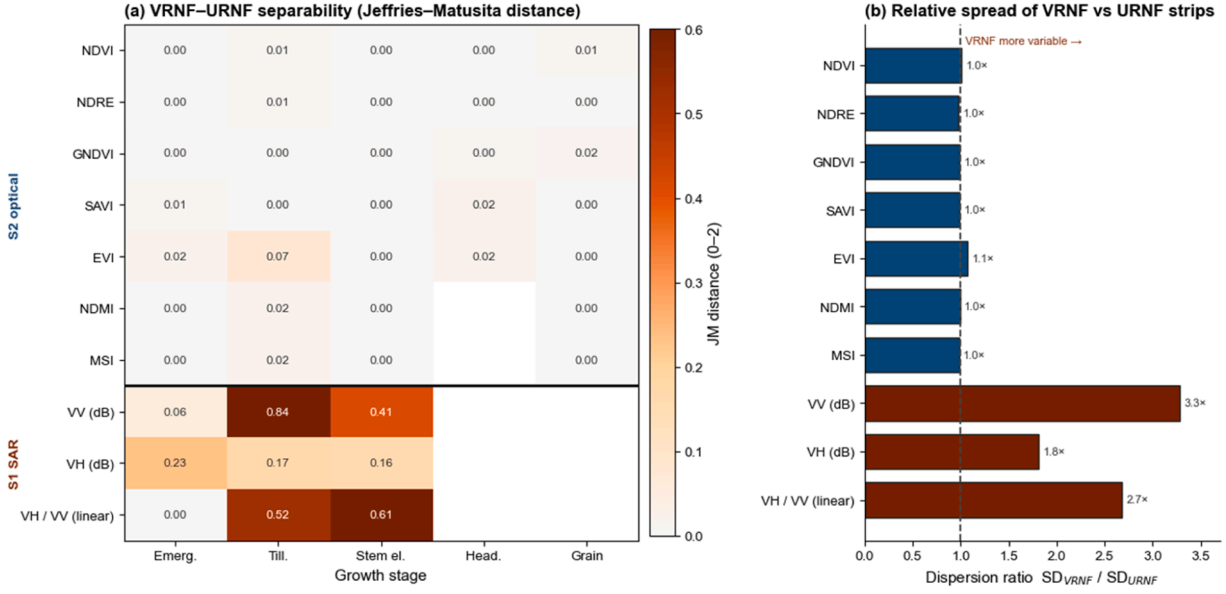


Fig. C.1. Treatment separability of Sentinel-1 (S1) synthetic aperture radar (SAR) and Sentinel-2 (S2) optical metrics between variable-rate and uniform-rate nitrogen fertilizer (VRNF and URNF) application across the winter barley growing season in Òdena (Catalonia, Spain), 2024–2025. (a) Jeffries-Matusita (JM) distance (range 0–2) between VRNF and URNF strip-level medians, computed per band and phenological stage (Emerg., emergence/early tillering; Till., tillering; Stem el., stem elongation; Head., heading/anthesis; Grain, grain filling). Optical indices: NDVI, Normalised Difference Vegetation Index; NDRE, Normalised Difference Red-Edge Index; GNDVI, Green NDVI; SAVI, Soil-Adjusted Vegetation Index; EVI, Enhanced Vegetation Index; NDMI, Normalised Difference Moisture Index; MSI, Moisture Stress Index. SAR metrics: VV and VH backscatter (dB) and the VH/VV ratio (linear). (b) Dispersion ratio (SD_{VRNF}/SD_{URNF}), the ratio of the standard deviation of VRNF to URNF strip medians, averaged over the season; values >1 indicate greater variability among VR strips. No band-stage combination differed significantly in central tendency (Mann-Whitney U, $p > 0.05$); VRNF-URNF separability is therefore dispersion-driven. VR pools five N levels (50–150% of the recommended reference rate R), so treatment means coincide with UR by design.

Appendix D

Table D.1
Site specific nitrogen (N) rate and yield by vriable rate N fertilisation (VRNF) under the kings (VRNF-KS) and Robin Hood (VRNF-RHS) schemes at the three study sites (2024–2025).

VR treatment	Area (ha)	N rate (L ha^{-1})	± % from *R*	Yield (t ha^{-1})
VRNF-KS, variable-rate targeted strategy (higher N to high-fertility zones)				
VR-L (KS)	1.09	102	50%	7.18
VR-ML (KS)	1.21	152	75%	7.61
VR-M (KS)	0.98	203	100%	7.74
VR-MH (KS)	1.14	254	125%	7.68
VR-H (KS)	0.45	305	150%	7.22
Weighted mean	4.88	189	—	7.52
VRNF-RHS, variable-rate compensative strategy (higher N to low-fertility zones)				
VR-L (RHS)	1.04	305	150%	7.88
VR-ML (RHS)	0.17	254	125%	8.00
VR-M (RHS)	0.98	203	100%	7.74
VR-MH (RHS)	1.35	152	75%	8.07
VR-H (RHS)	0.58	102	50%	7.99
Weighted mean	4.12	200	—	7.93
R (ref.)	4.56	203	100%	7.72

Weighted field means correspond to the Total VR yield values reported in Table 6. VR rate zones: VR-L / ML / M / MH / H = low / medium-low / medium / medium-high / high N application rate. farmer rate R (ref.) is the uniform-rate control.

Data availability

https://dataspace.copernicus.eu/ (The Sentinel-1 synthetic aperture radar (SAR) data and Sentinel-2 multispectral imagery used in this study are freely available from the Copernicus programme (European Space Agency,) using the standard open-access licence. The rest of the datasets supporting this study can be obtained from the authors upon request.)

References

[1] M. Anas, F. Liao, K.K. Verma, M.A. Sarwar, A. Mahmood, Z.L. Chen, Q. Li, X. P. Zeng, Y. Liu, Y.R. Li, Fate of nitrogen in agriculture and environment: agronomic, eco-physiological and molecular approaches to improve nitrogen use efficiency, Biol. Res. 53 (1) (2020), https://doi.org/10.1186/s40659-020-00312-4.

[2] X. Zhang, E.A. Davidson, D.L. Mauzerall, T.D. Searchinger, P. Dumas, Y. Shen, Managing nitrogen for sustainable development, Nature 528 (7580) (2015) 51–59, https://doi.org/10.1038/nature15743.

[3] L. You, G.H. Ros, Y. Chen, Q. Shao, M.D. Young, F. Zhang, W. de Vries, Global mean nitrogen recovery efficiency in croplands can be enhanced by optimal nutrient, crop and soil management practices, Nat. Commun. 14 (1) (2023), https://doi.org/10.1038/s41467-023-41504-2.

[4] Z. Zhai, J.F. Martínez, V. Beltran, N.L. Martínez, Decision support systems for agriculture 4.0: survey and challenges, Comput. Electron. Agric. 170 (2020), https://doi.org/10.1016/j.compag.2020.105256.

[5] European Commission, Common Agricultural Policy 2023-2027: CAP Strategic Plans, 2022. https://ec.europa.eu/commission/presscorner/detail/en/ip_22_5183.

[6] N. Amangeldy, A. Guerrero, H. Luo, M.A. Munnaf, G. Haesaert, E. Meers, A. M. Mouazen, Variable-rate bio-based nitrogen fertilization in grain maize: field evaluations in Belgium, Nutr. Cycl. Agroecosyst. 133 (1) (2026), https://doi.org/10.1007/S10705-026-10509-W.

[7] A. Guerrero, S. De Neve, A.M. Mouazen, Data fusion approach for map-based variable-rate nitrogen fertilization in barley and wheat, Soil Till. Res. 205 (2021) 104789, https://doi.org/10.1016/j.still.2020.104789.

[8] A. Guerrero, A.M. Mouazen, Evaluation of variable rate nitrogen fertilization scenarios in cereal crops from economic, environmental and technical perspective, Soil Till. Res. 213 (2021) 105110, https://doi.org/10.1016/j.still.2021.105110.

[9] S. Hamed Javadi, A. Guerrero, A.M. Mouazen, Clustering and smoothing pipeline for management zone delineation using proximal and remote sensing, Sensors 22 (2) (2022) 645, https://doi.org/10.3390/s22020645.

[10] A. Patricia, G. Castillo, Site-Specific Nitrogen Fertilization based on Proximal and Remote Sensing Technologies, 2022.

[11] J. Zhang, A. Guerrero, A.M. Mouazen, Map-based variable-rate manure application in wheat using a data fusion approach, Soil Till. Res. 207 (2021) 104846, https://doi.org/10.1016/j.still.2020.104846.

[12] U. Ahmad, A. Nasirahmadi, O. Hensel, S. Marino, Technology and data fusion methods to enhance site-specific crop monitoring, Agronomy 12 (3) (2022), https://doi.org/10.3390/agronomy12030555.

[13] C. Toth, G. Jóźków, Remote sensing platforms and sensors: a survey, ISPRS J. Photogramm. Remote Sens. 115 (2016) 22–36, https://doi.org/10.1016/j.isprsjprs.2015.10.004.

[14] E. Beriaux, A. Jago, C. Lucau-Danila, V. Planchon, P. Defourny, Sentinel-1 time series for crop identification in the framework of the future cap monitoring, Remote Sens. 13 (14) (2021) 2785, https://doi.org/10.3390/rs13142785.

[15] A. Moreira, P. Prats-Iraola, M. Younis, G. Krieger, I. Hajnsek, K.P. Papathanassiou, A. Moreira, P. Prats-Iraola, M. Younis, G. Krieger, I. Hajnsek, K.P. Papathanassiou, Alberto Moreira, Pau Prats-Iraola, Marwan Younis, Krieger, K. P, A tutorial on synthetic aperture radar, IGRSM 1 (1) (2013) 6–43, https://doi.org/10.1109/MGRS.2013.2248301.

[16] M. De Vroey, L. de Vendictis, M. Zavagli, S. Bontemps, D. Heymans, J. Radoux, B. Koetz, P. Defourny, Mowing detection using Sentinel-1 and Sentinel-2 time series for large scale grassland monitoring, Remote Sens. Environ. 280 (2022) 113145, https://doi.org/10.1016/j.rse.2022.113145.

[17] C. Gómez, J.C. White, M.A. Wulder, Optical remotely sensed time series data for land cover classification: a review, ISPRS J. Photogramm. Remote Sens. 116 (2016) 55–72, https://doi.org/10.1016/j.isprsjprs.2016.03.008.

[18] X.P. Song, W. Huang, M.C. Hansen, P. Potapov, An evaluation of Landsat, Sentinel-2, Sentinel-1 and MODIS data for crop type mapping, Sci. Remote Sens. 3 (2021) 100018, https://doi.org/10.1016/j.srs.2021.100018.

[19] N. Amangeldy, K.H.E. Meurer, U. Franko, H. Luo, E. Meers, A.M. Mouazen, Integrating decision support systems for site-specific application of bio-based fertilizers: a review, Precis. Agric. 27 (5) (2026) 121, https://doi.org/10.1007/S11119-026-10422-W.

[20] R.G. Pontius, M.L. Cheuk, A generalized cross-tabulation matrix to compare soft-classified maps at multiple resolutions, Int. J. Geograph. Inf. Sci. 20 (1) (2006) 1–30, https://doi.org/10.1080/13658810500391024.

[21] R.G. Pontius, M. Millones, Death to Kappa: birth of quantity disagreement and allocation disagreement for accuracy assessment, Int. J. Remote Sens. 32 (15) (2011) 4407–4429, https://doi.org/10.1080/01431161.2011.552923.

[22] European Union, CORINE Land Cover 2018 (Spain), 2018. https://data.europa.eu/data/datasets/spaignclc2018?locale=en.

[23] Servei Meteorològic de Catalunya. Dades de l'estació automàtica Òdena, Meteocat, 2024. https://www.meteo.cat/observacions/xema/dades?codi=H1.

[24] A. Mouazen, Soil Survey Device (Patent WO2006/015463; PCT/BE2005/000129), World Intellectual Property Organization, 2006.

[25] G.P. Gillman, D.C. Burkett, R.J. Coventry, A laboratory study of application of basalt dust to highly weathered soils: effect on soil cation chemistry, Austral. J. Soil Res. 39 (4) (2001) 799–811, https://doi.org/10.1071/SR00073.

[26] S.K. Gupta, I.C. Gupta, Genesis and Management of Sodic (Alkali) Soils, Scientific Publishers, 2017.

[27] International Organization for Standardization, Soil Quality—Determination of Particle Size Distribution in Mineral Soil Material—Method by Sieving and Sedimentation, 2020. ISO No. 11277:2020, https://www.iso.org/standard/69496.html.

[28] A.M. Mouazen, H. Ramon, Expanding implementation of an on-line measurement system of topsoil compaction in loamy sand, loam, silt loam and silt soils, Soil Till. Res. 103 (1) (2009) 98–104, https://doi.org/10.1016/j.still.2008.09.012.

[29] R.J Barnes, M.S Dhanoa, S.J. Lister, Standard normal variate transformation and de-trending of near-infrared diffuse reflectance spectra, Appl. Spectrosc. 43 (5) (1989) 772–777, https://doi.org/10.1366/0003702894202201.

[30] R.W. Kennard, L.A. Stone, Computer aided design of experiments, Technometrics 11 (1) (1969) 137–148, https://doi.org/10.1080/00401706.1969.10490666.
[31] V. Bellon-Maurel, E. Fernandez-Ahumada, B. Palagos, J.M. Roger, A. McBratney, Critical review of chemometric indicators commonly used for assessing the quality of the prediction of soil attributes by NIR spectroscopy, TrAC Trends Anal. Chem. 29 (9) (2010) 1073–1081, https://doi.org/10.1016/J.TRAC.2010.05.006.
[32] S. Nawar, A.M. Mouazen, S. Nawar, A.M. Mouazen, Predictive performance of mobile vis-near infrared spectroscopy for key soil properties at different geographical scales by using spiking and data mining techniques, Caten 151 (2017) 118–129, https://doi.org/10.1016/J.CATENA.2016.12.014.
[33] N. Amangeldy, W. Riegler, A.M. Mouazen, Optimized automatic prediction of online vis-NIR soil spectra: comparison of three neural network models. Precision Agriculture '25, 2025, https://doi.org/10.1163/9789004725232_176.
[34] N. Gorelick, M. Hancher, M. Dixon, S. Ilyushchenko, D. Thau, R. Moore, Google Earth Engine: planetary-scale geospatial analysis for everyone, Remote Sens. Environ. 202 (2017) 18–27, https://doi.org/10.1016/j.rse.2017.06.031.
[35] ESA, Sentinel-2 User Handbook, 2013.
[36] R.P. Sishodia, R.L. Ray, S.K. Singh, Applications of remote sensing in precision agriculture: a review, Remote Sens. 12 (19) (2020) 3136, https://doi.org/10.3390/rs12193136.
[37] Rouse, J.W., Jr., Haas, R.H., Deering, D.W., Schell, J.A., & Harlan, J.C. (1973). Monitoring the vernal advancement and retrogradation (green wave effect) of natural vegetation. [Great Plains Corridor].
[38] Barnes, E., Clarke, T., Richards, S., Colaizzi, P., Haberland, J., Kostrzewski, M., Waller, P., Choi, C., Riley, E., Thompson, T., Lascano, R.J., Li, H., Moran, M.S., Robert, P.C., Rust, R.H., & Larson, W.E. (2000). Coincident detection of crop water stress, nitrogen status and canopy density using ground-based multispectral data. 5th International conference on Precision Agriculture, Bloomington, 16-19 July 2000, p. 1-15.
[39] A. Huete, K. Didan, T. Miura, E.P. Rodriguez, X. Gao, L.G. Ferreira, Overview of the radiometric and biophysical performance of the MODIS vegetation indices, Remote Sens. Environ. 83 (2002) 195–213, https://doi.org/10.1016/S0034-4257(02)00096-2.
[40] A.A. Gitelson, Y.J. Kaufman, M.N. Merzlyak, J. Blaustein, Use of a green channel in remote sensing of global vegetation from EOS-MODIS, Remote Sens. Environ. 58 (1995).
[41] A.R. Huete, A soil-adjusted vegetation index (SAVI), Remote Sens. Environ. 25 (3) (1988) 295–309, https://doi.org/10.1016/0034-4257(88)90106-X.
[42] B. Gao, NDWI - A normalized difference water index for remote sensing of vegetation liquid water from space, Remote Sens. Environ. 7212 (1996).
[43] E. Koohikeradeh, S. Jose Gumiere, H. Bonakdari, NDMI-derived field-scale soil moisture prediction using ERA5 and LSTM for precision agriculture, Sustainability 17 (6) (2025) 2399, https://doi.org/10.3390/su17062399.
[44] A. Holik, W. Tian, A. Psilovikos, M. Elhag, Towards a near-real-time water stress monitoring system in tropical heterogeneous landscapes using remote sensing data, Hydrology 12 (12) (2025) 325, https://doi.org/10.3390/hydrology12120325.
[45] E.R. Hunt, B.N. Rock, Detection of changes in leaf water content using near- and middle-infrared reflectances, Remote Sens. Environ. 30 (1) (1989) 43–54, https://doi.org/10.1016/0034-4257(89)90046-1.
[46] P. Dusseux, T. Guyet, P. Pattier, V. Barbier, H. Nicolas, Monitoring of grassland productivity using Sentinel-2 remote sensing data, Int. J. Appl. Earth Observ. Geoinf. 111 (2022) 102843, https://doi.org/10.1016/J.JAG.2022.102843.
[47] M. Lamichhane, S. Mehan, K.R. Mankin, Surface soil moisture prediction using multimodal remote sensing data fusion and machine learning algorithms in semi-arid agricultural region, Sci. Remote Sens. 12 (2025) 100255, https://doi.org/10.1016/j.srs.2025.100255.
[48] X. Zhu, Q. Li, C. Guo, Evaluation of the monitoring capability of various vegetation indices and mainstream satellite band settings for grassland drought, Ecol. Inform. 82 (2024) 102717, https://doi.org/10.1016/J.ECOINF.2024.102717.
[49] K. Hogenson, H. Kristenson, J. Kennedy, A. Johnston, J. Rine, T. Logan, J. Zhu, F. Williams, J. Herrmann, J. Smale, F. Meyer, Hybrid Pluggable Processing Pipeline (HyP3): a cloud-native infrastructure for generic processing of SAR data, Zenodo (2024), https://doi.org/10.5281/zenodo.10903242.
[50] J.S. Lee, J.H. Wen, T.L. Ainsworth, K.S. Chen, A.J Chen, Improved sigma filter for speckle filtering of SAR imagery, IEEE Trans. Geosci. Remote Sens. 47 (1) (2009) 202–213, https://doi.org/10.1109/TGRS.2008.2002881.
[51] J. Sardans, J. Peñuelas, Plant-soil interactions in Mediterranean forest and shrublands: impacts of climatic change, Plant Soil 365 (1–2) (2013) 1–33, https://doi.org/10.1007/s11104-013-1591-6.
[52] S. Thenkabail, Y. Miao, Y. Huang, Q. Cao, C. Yang, K. Kusnierek, X. Sun, M. Abdul Munnaf, A. Guerrero, M. Calera, A. Mounem Mouazen, Precision nitrogen fertilization for Opium Poppy using combined proximal and remote sensor data fusion, Remote Sens. 15 (23) (2023) 5442, https://doi.org/10.3390/RS15235442.
[53] M.A. Munnaf, G. Haesaert, A.M. Mouazen, Map-based site-specific seeding of seed potato production by fusion of proximal and remote sensing data, Soil Till. Res. 206 (2021) 104801, https://doi.org/10.1016/j.still.2020.104801.
[54] M. Diacono, A. Castrignanò, A. Troccoli, D. De Benedetto, B. Basso, P. Rubino, Spatial and temporal variability of wheat grain yield and quality in a Mediterranean environment: a multivariate geostatistical approach, Field. Crops. Res. 131 (2012) 49–62, https://doi.org/10.1016/j.fcr.2012.03.004.
[55] J.A. Doolittle, E.C. Brevik, The use of electromagnetic induction techniques in soils studies, Geoderma 223-225 (1) (2014) 33–45, https://doi.org/10.1016/j.geoderma.2014.01.027.
[56] F.J. Moral, J.M. Terrón, J.R.M. da Silva, Delineation of management zones using mobile measurements of soil apparent electrical conductivity and multivariate geostatistical techniques, Soil Till. Res. 106 (2) (2010) 335–343, https://doi.org/10.1016/j.still.2009.12.002.
[57] G.M. Foody, Status of Land Cover Classification Accuracy Assessment, 2001. www.elsevier.com/locate/rse.
[58] O.G. Varga, R.G. Pontius, S.K. Singh, S. Szabó, Intensity analysis and the Figure of Merit's components for assessment of a Cellular Automata – Markov simulation model, Ecol. Indic. 101 (2019) 933–942, https://doi.org/10.1016/j.ecolind.2019.01.057.
[59] A. Tsitouras, C. Noulas, V. Liakos, S. Stamatiadis, M. Tziouvalekas, R. Qin, E. Evangelou, Variable-rate nitrogen application in wheat based on UAV-derived fertilizer maps and precision agriculture technologies, Agronomy 15 (7) (2025) 1714, https://doi.org/10.3390/agronomy15071714.
[60] Y. Wang, Y. Yuan, F. Yuan, S.T. Ata-UI-Karim, X. Liu, Y. Tian, Y. Zhu, W. Cao, Q. Cao, Evaluation of variable application rate of fertilizers based on site-specific management zones for winter wheat in small-scale farming, Agronomy 13 (11) (2023) 2812, https://doi.org/10.3390/agronomy13112812.
[61] A. de Lara, T. Mieno, J.D. Luck, L.A. Puntel, Predicting site-specific economic optimal nitrogen rate using machine learning methods and on-farm precision experimentation, Precis. Agric. 24 (5) (2023) 1792–1812, https://doi.org/10.1007/s11119-023-10018-8.